

## The role of fluctuations in bistability and oscillations during the $\text{H}_2+\text{O}_2$ reaction on nanosized rhodium crystals

P. Grosfils and P. Gaspard

*Center for Nonlinear Phenomena and Complex Systems (CENOLI),  
Université libre de Bruxelles (ULB), Campus Plaine  
Code Postal 231, B-1050 Brussels, Belgium*

T. Visart de Bocarmé

*Center for Nonlinear Phenomena and Complex Systems (CENOLI) and  
Chemical Physics of Materials – Catalysis and Tribology,  
Université libre de Bruxelles (ULB), Campus Plaine  
Code Postal 243, B-1050 Brussels, Belgium*

A combined experimental and theoretical study is presented of fluctuations observed by field ion microscopy in the catalytic reaction of water production on a rhodium tip. A stochastic approach is developed to provide a comprehensive understanding of the different phenomena observed in the experiment, including burst noise manifesting itself in a bistability regime, noisy oscillations, and nanopatterns with a cross-like oxidized zone separating the surface into four quadrants centered on the  $\{111\}$  facets. The study is based on a stochastic model numerically simulating the processes of adsorption, desorption, reaction, and transport. The surface diffusion of hydrogen is described as a percolation process dominated by large clusters corresponding to the four quadrants. The model reproduces the observed phenomena in the ranges of temperature, pressures, and electric field of the experiment.

### I. INTRODUCTION

At the macroscale, nonlinear phenomena such as bistability, oscillations, or spatiotemporal patterns emerge in reaction-diffusion systems driven far from equilibrium [1–4]. These phenomena are neatly observed in heterogeneous catalysis on planar crystalline surfaces in contact with gas mixtures of reactants at low pressures where the distance from equilibrium is controlled by the ratio of reactant-to-product partial pressures. In particular, oscillations as well as spiral waves have been observed and studied in great detail for the oxidation of carbon monoxide on platinum [5–8]. Oscillations have also been observed on non-planar surfaces in further catalytic reactions, e.g., the formation of water on palladium, platinum, and rhodium, or the hydrogenation of  $\text{NO}_2$  on platinum [7–9]. In this context, a fundamental preoccupation is to know how these nonlinear phenomena can emerge at the macroscale from the atomic structure of matter.

At the nanoscale, thermal and molecular fluctuations – due to the incessant and random motions of atoms – strongly affect reactions and transport of matter. This is the case for the catalytic formation of water on rhodium as observed by field ion microscopy (FIM) [10, 11]. In such circumstances, the process takes place on metallic tips in the presence of a high electric field, allowing the observation of the reaction with a nanometric resolution. Thanks to such microscopy techniques, bistability and self-sustained oscillations have been discovered and investigated in this system [10, 11], as well as in other surface reactions [12–18]. In these experiments, patterns are observed that are common to the bistable and oscillatory regimes and that find their origin in the underlying crystalline structure, which modulates the rate constants on the non-planar surface of the tip. The smaller the size of the system, the stronger the fluctuations. Accordingly, oscillations are no longer strictly periodic and the deterministic steady states lose their stationarity. Such effects are especially important in bistability where the fluctuations may induce transitions from states that would otherwise remain stable [19–30]. Although these phenomena have been theoretically investigated in bistable systems that are uniform [31, 32] or composed of two facets [33], the challenging issue is to understand the effects of fluctuations in catalytic reactions taking place on the multifaceted anisotropic surface of a field emitter tip in the presence of a strongly nonuniform electric field.

The purpose of the present paper is to address this issue by a combined experimental and theoretical study of fluctuations in the catalytic reaction of water production on a rhodium nanosized crystal exposed to low pressures of dihydrogen and dioxygen. In a series of previous papers [34–36], we have carried out the theoretical modeling of this system with deterministic kinetic equations in the absence of fluctuations. This modeling provides a global description of different features, including in particular the geometry of the field emitter tip and its multifaceted

surface, the spatial modulation of the rate constants due to the high electric field and the anisotropy coming from the underlying crystal, and the formation of a surface oxide trilayer O(ad)-Rh-O(sub), which plays a key role in the reaction on rhodium. Moreover, this global model is consistent with data from spectra of temperature-programmed desorption [36]. Here, our aim is to proceed with a stochastic approach extending our global model in order to explain the observed erratic fluctuations particularly in the bistable regime. If the fluctuations already affect the oscillations, which become noisy and decorrelated by phase diffusion, the effect is even more crucial in the bistable regime where the system becomes time dependent, randomly switching back and forth between the hydrogen- and oxygen-covered states of the surface. The experimental observations reveal a remarkable decoupling between the four quadrants that are developed over a (001)-oriented field emitter tip. Accordingly, they undergo random transitions independently of each other between both states. A central issue is the ultrafast surface diffusion of hydrogen, which tends to couple together the four quadrants. In order to explain the observed phenomenon, the surface diffusion of hydrogen should be assumed to be much reduced in the oxygen-covered regions of the surface, which generates a mechanism of percolation of hydrogen if the oxygen coverage reaches some threshold. In this way, the decoupling observed in the bistable regime between the four quadrants can be explained, as we show in the present paper.

The paper is organized as follows. The experimental observations are reported in Section II. The model of the field emitter tip is introduced in Section III and the reaction scheme in Section IV. Hydrogen surface diffusion and percolation on an oxygen-covered surface is discussed in Section V. The stochastic algorithm and its master equation are explained in Section VI. The results on the oscillatory regime are presented in Section VII and those on the regime of bistability in Section VIII. Conclusions are drawn in Section IX.

## II. EXPERIMENTAL OBSERVATIONS

### A. The experimental setup

The reaction is observed with nanoscale resolution thanks to a video-FIM device described in detail elsewhere [37]. The field emitter tip is prepared with rhodium in the form of a nearly hemispherical shape with a radius of curvature at the apex of 10-20 nm. The orientation of the underlying rhodium crystal is first determined by imaging its surface under FIM conditions at cryogenic temperature with neon. Thereafter, the video-FIM is operated as a flow reactor while imaging the dynamical behavior with nanometric lateral resolution between 400 K and 600 K at a fixed oxygen pressure  $P_{O_2}$  and varying values of hydrogen pressure  $P_{H_2}$ . All gas pressures are measured with an ion gauge and corrected for ion gauge sensitivity. Standard FIM images are taken with a high dynamic range CCD camera ( $512 \times 512$  pixels, 16 bits per pixel). Video sequences have been recorded using a high sensitivity camera with a time resolution of 20 ms. The electric field at the apex is in the range 10-15 V/nm. Imaging is generated by water cations  $H_2O^+$  and  $H_3O^+$  [11]. Ionization only perturbs weakly the populations of neutral species so that ionization is passively driven by the time evolution of neutral species. Since water formation requires the presence of hydrogen, the brightness of FIM images is higher in hydrogen-covered than oxygen-covered surface areas.

### B. Bistability and oscillations

For small  $P_{H_2}/P_{O_2}$  ratios, the surface is predominantly covered by oxygen, either as adsorbed monoatomic oxygen, or in the form of a surface oxide of stoichiometry  $Rh_xO_y$ . For large  $P_{H_2}/P_{O_2}$  ratios, the surface is mainly covered by hydrogen. For intermediate values of the ratio, the system becomes bistable with hysteresis extending over a certain range of  $P_{H_2}/P_{O_2}$  that is decreasing as the temperature increases from 400 K to 525 K. Oscillatory behaviors are observed around 550 K, which have been analyzed elsewhere [34–36].

### C. Bistability and noise

In this paper, we focus on the hysteretic behavior, which is strongly affected by thermal and molecular fluctuations. With a (001) facet located at the apex of the tip, the observation shows the formation of four quadrants centered on the four facets (111), ( $\bar{1}11$ ), ( $1\bar{1}1$ ), and ( $1\bar{1}\bar{1}$ ), as depicted in Fig. 1. These quadrants are separated from each other by a cross-like zone including the apex and the four facets (101), (011), ( $\bar{1}01$ ), and ( $0\bar{1}1$ ). This cross-like zone remains covered by oxygen or its surface oxide. In contrast, the four quadrants undergo random transitions between the hydrogen-covered and oxygen-covered surface states, as observed in Fig. 2. Although bistability would be expected in this regime for macroscopic systems, the thermal and molecular fluctuations due to the small size of the system cause the metastability of both states, and induce random transitions between them in the course of time. These

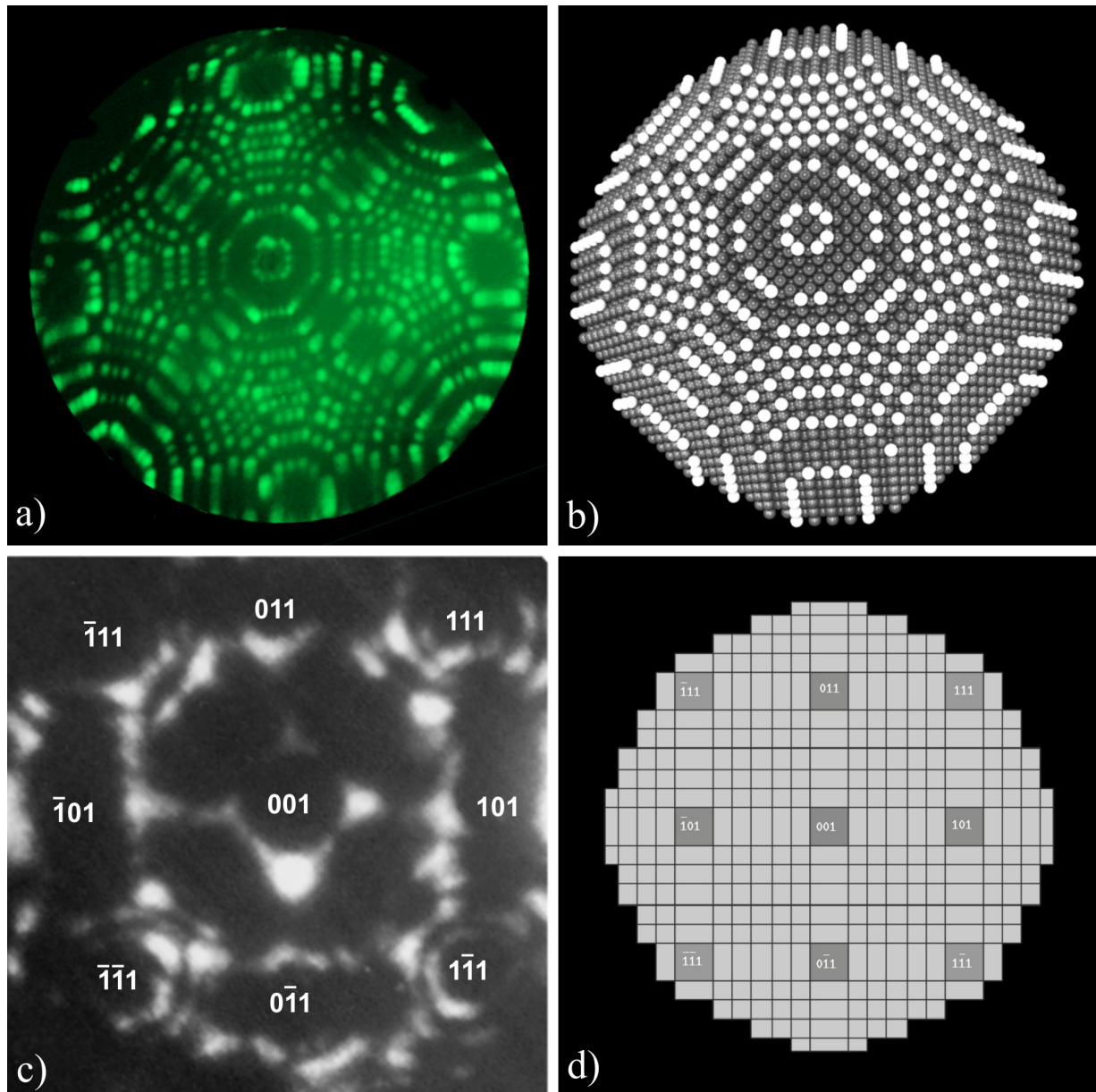


FIG. 1: (a) Field ion micrograph of a (001)-oriented Rh tip sample imaged at  $T = 50$  K in the presence of neon gas ( $P_{\text{Ne}} = 10^{-3}$  Pa,  $F_0 = 35$  V/nm). (b) Ball model of a face-centred cubic (fcc) crystal given the form of a quasi-hemisphere depicting the situation encountered in (a). Each ball represents one single atom; the white balls figure the most protruding atoms of the tip sample. (c) Field ion microscopy of a (001)-oriented Rh tip sample during the ongoing exposure to a reactive  $\text{H}_2 + \text{O}_2$  gas mixture ( $T = 550$  K,  $P_{\text{H}_2} = 1.3 \times 10^{-3}$  Pa,  $P_{\text{O}_2} = 1.0 \times 10^{-3}$  Pa,  $F_0 = 12.3$  V/nm). (d) Top view of the facet model for comparison with (c).

transitions manifest themselves at the level of the brightness, which is shown as a function of time in Fig. 3. In this case, the observed quadrant randomly switches between the bright H-covered state and the dark O-covered state, generating burst noise as in a random telegraph signal. Although transformed into metastability by the fluctuations, we shall continue to refer to this regime as bistable as long as two distinct states can be identified in the time series. In Fig. 3 for instance, the dwell time is on average 4.8 s to remain in the bright H-covered state, and 1.5 s in the dark O-covered state. These dwell time intervals are separated by random jumps between the two states. The jumps last about 0.5 s.

Furthermore, the four quadrants are observed in Fig. 2 to switch randomly between both H-covered and O-covered states independently of each other. One quadrant may switch although its neighbors do not. The data do not show statistically significant cross-correlations between the quadrants given the recorded time series.

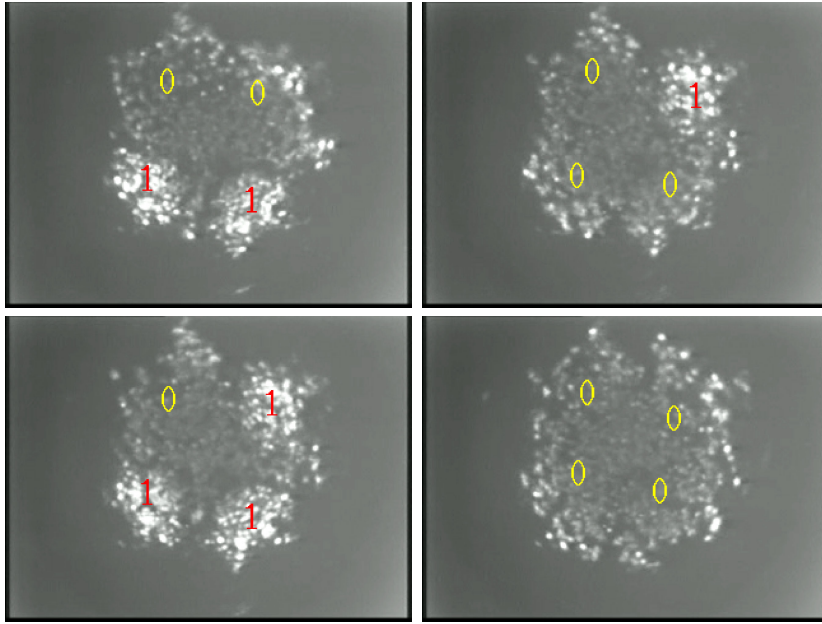


FIG. 2: Series of micrographs as part of a video sequence showing the surface in the bistable regime at 450 K,  $P_{O_2} = 5.0 \times 10^{-4}$  Pa,  $P_{H_2}/P_{O_2} = 10.0$ , and  $F_0 = 12.3$  V/nm. The surface composition in each one of the four quadrants fluctuates between the hydrogen-covered surface state (1) and the oxygen-covered surface state (0).

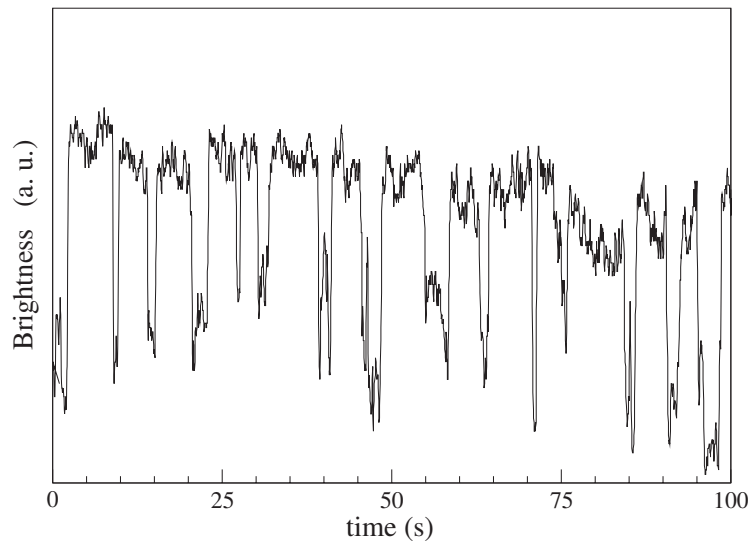


FIG. 3: Time evolution of the brightness in one quadrant of the tip surface extracted from a video sequence of the surface in the bistable regime at 450 K,  $P_{O_2} = 5.0 \times 10^{-4}$  Pa,  $P_{H_2}/P_{O_2} = 10.0$ , and  $F_0 = 12.3$  V/nm.

#### D. Front propagation during transitions

On shorter time scales, another time-dependent phenomenon is observed. In Fig. 4, the bright hydrogen-covered state in the lower left quadrant is seen to propagate in the direction of the apex of the tip when the quadrant switches from the oxygen- to the hydrogen-covered state. This phenomenon repeats itself every time a quadrant undergoes a switch, as we can see in the animated movie attached to Fig. 4. The propagation happens on the time scale of the sudden transitions between both states. A remarkable feature is that the direction of propagation is the same under similar conditions.

The understanding of these time-dependent phenomena requires a stochastic approach beyond the deterministic kinetic scheme, as presented in the following.

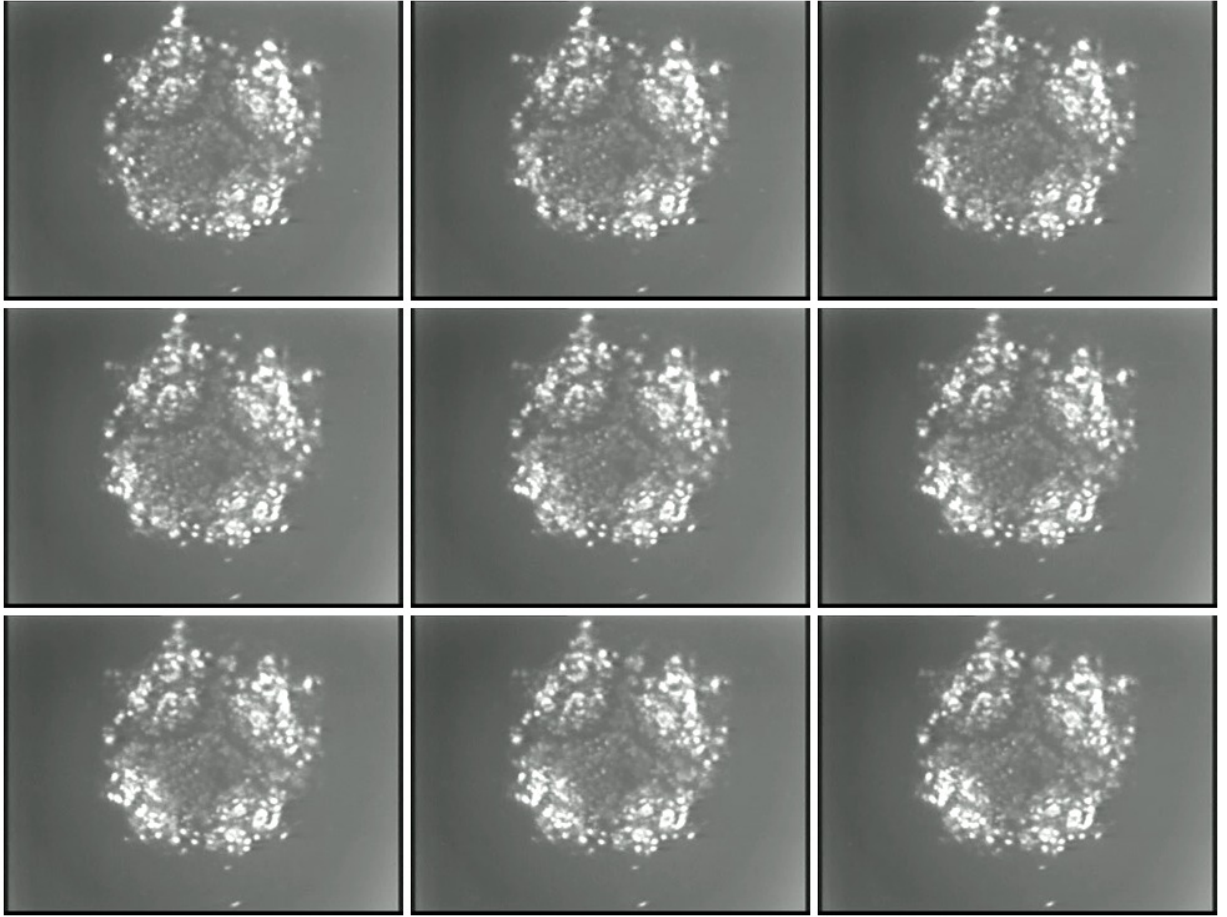


FIG. 4: Series of micrographs as part of a video sequence (from left to right and from top to bottom) showing the propagation of the hydrogen-covered state towards the apex in the lower left quadrant, which becomes brighter as time increases. The system is in the bistable regime at 450 K,  $P_{\text{O}_2} = 5.0 \times 10^{-4}$  Pa,  $P_{\text{H}_2}/P_{\text{O}_2} = 10.0$ , and  $F_0 = 12.3$  V/nm. The sampling time is here  $\Delta t = 40$  ms. (Multimedia view)

### III. MODEL OF THE FIELD EMITTER TIP

#### A. Geometry

The rhodium tip is modeled as a paraboloid

$$z = \frac{R}{2} - \frac{x^2 + y^2}{2R}, \quad (1)$$

with a radius of curvature at the apex equal to  $R \simeq 19$  nm. It is cut in a face-centered cubic (fcc) crystal of lattice constant  $a = 3.8$  Å. The axis of the paraboloid is oriented in the direction [001] so that a (001) facet is formed at the apex.

The modeling is carried out at the mesoscopic level of description on scales just larger than the atomic one. With this purpose, the surface is coarse grained into fictitious facets that are small enough to describe spatially dependent phenomena and sufficiently large to contain each one more than a dozen of surface atomic sites, as shown in Fig. 5. The facets of the grid (seen in Fig. 5b) are constructed such that their projection into the  $xy$ -plane are the rectangles shown in Fig. 1d. The number of these facets is equal to  $n = 305$ . We emphasize the fact that these facets are fictitious and do not necessarily correspond to the facets formed by cutting the crystal in a paraboloidal shape. Indeed, the facets of the grid are rectangular, while the real facets (seen in the ball model of Fig. 5a) are ovoidal such as (001), (111), ( $\bar{1}11$ ), ( $1\bar{1}1$ ), etc...

In order to calibrate the model with respect to the atomic scale, the numbers  $\{N_i\}_{i=1}^n$  of sites in each facet of the grid are counted with the ball model depicted in Fig. 5a. These numbers are given in Table I for the main facets, if

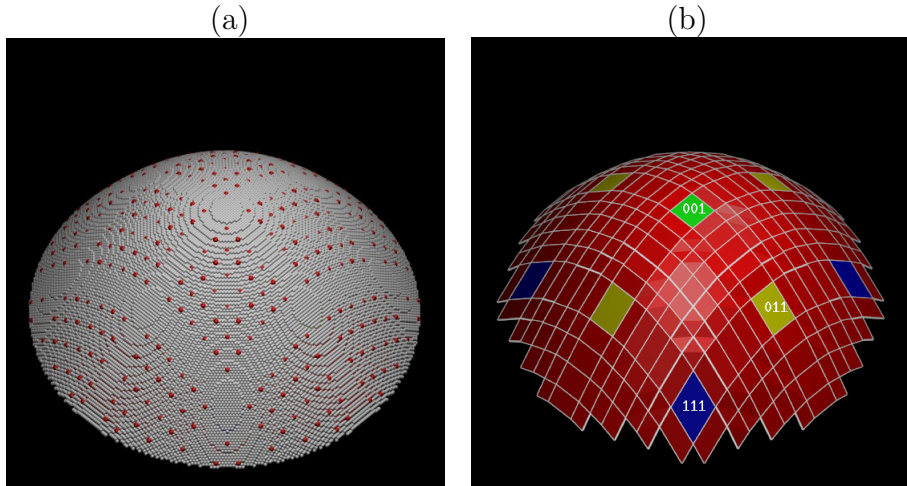


FIG. 5: (a) Ball model of a paraboloidal [001]-oriented fcc crystal. The radius of curvature is 19 nm. The atoms painted in dark color (red) are the corners of small facets of different Miller indices. (b) Facet model based on the ball model. The positions of the dark (red) atoms in (a) are the grid points that delimit the 305 small facets of the model.

$R = 19$ nm	$R = 15$ nm
$N_{\text{tot}} = 44885$	$N_{\text{tot}} = 27426$
$N(001) = 284$	$N(001) = 145$
$N(011) = 401$	$N(011) = 225$
$N(111) = 490$	$N(111) = 303$
$N(117) = 73$	$N(117) = 54$
$N(227) = 79$	$N(227) = 40$
$N(112) = 113$	$N(112) = 62$
$N(447) = 96$	$N(447) = 69$
$N(557) = 106$	$N(557) = 77$

TABLE I: Numbers of atomic sites in the main facets of grids covering paraboloidal tips of curvature radii  $R$ .  $N_{\text{tot}}$  denotes the total number of atomic sites on the modeled part of the tips (shown in Fig. 5b for  $R = 19$  nm).

the radius of curvature is  $R = 19$  nm and  $R = 15$  nm. The total number of atomic sites on the modeled part of the tip is equal to  $N_{\text{tot}} = \sum_{i=1}^n N_i$ .

The stochastic process is followed at the level of the random numbers of hydrogen adatoms, oxygen adatoms, and subsurface oxygen atoms in every one of these facets:  $\{H_i, O_i, S_i\}_{i=1}^n$ . These numbers change in time at random events of adsorption, desorption, surface diffusion, and reaction, according to the kinetic scheme detailed here below. The local coverages or mean occupation numbers in the facets are defined as

$$0 \leq \theta_{\text{H}} = \frac{H_i}{N_i} \leq 1, \quad 0 \leq \theta_{\text{O}} = \frac{O_i}{N_i} \leq 1, \quad 0 \leq \theta_{\text{S}} = \frac{S_i}{N_i} \leq 1. \quad (2)$$

The so-defined coverages are common to all the surface orientations, which is suitable to deal with a multifaceted surface [35, 36]. The surface density of the species can be estimated by  $\sigma_{\text{X}} \simeq \theta_{\text{X}}/a_s$  with  $a_s = 10 \text{ \AA}^2$ .

## B. Electric field

Under FIM conditions, the metallic tip is set to a high electric voltage for the ionization of adsorbed species and their imaging on a fluorescent screen thanks to the huge magnification factor between the nanometric tip and the centimetric screen. Consequently, the electric field at the apex can reach values as high as  $F_0 = 10\text{-}15 \text{ V/nm}$  during reaction. The electric field is vanishing in the metal bulk and normal to the surface,  $\mathbf{F} = F\mathbf{n}$ , where  $\mathbf{n}$  is a unit vector

normal to the surface. Around the paraboloid (1), its magnitude takes the value

$$F = \frac{F_0}{\sqrt{1 + (r/R)^2}}, \quad (3)$$

where  $r = \sqrt{x^2 + y^2}$  is the radial distance with respect to the symmetry axis of the paraboloid [38]. The electric field reaches its maximal value  $F_0$  at the apex where the radius of curvature takes its smallest value  $R$  and it vanishes in the flanks of the tip as  $r \rightarrow \infty$ , i.e., as  $z \rightarrow -\infty$  according to Eq. (1).

### C. Gas pressures

Since dihydrogen and dioxygen molecules are polarizable, their pressure on the tip surface increases with the electric field as

$$P_{X_2}(F) = P_{X_2}(0) \exp(\beta \alpha_{X_2} F^2/2), \quad \text{for } X = \text{H or O}, \quad (4)$$

where  $\beta = (k_B T)^{-1}$  is the inverse of the thermal energy with Boltzmann's constant  $k_B$ ,  $P_{X_2}(0)$  is the pressure at the gauge far from the tip, and  $\alpha_{X_2}$  is the effective polarizability of the molecules [39, 40]:

$$\alpha_{\text{H}_2} \simeq 0.00057 \text{ eV nm}^2 \text{ V}^{-2}, \quad (5)$$

$$\alpha_{\text{O}_2} \simeq 0.0011 \text{ eV nm}^2 \text{ V}^{-2}. \quad (6)$$

The gas pressure is low enough that the mean free paths are longer than the size of the vessel. Accordingly, diffusive transport does not happen in the gas above the surface, but only by surface diffusion of adspecies.

## IV. KINETIC SCHEME

The rhodium surface catalyzes water formation thanks to the dissociative adsorption of dihydrogen and dioxygen from the gas, making the monoatomic adspecies ready for water formation.

### A. Rate constants

Because of the crystalline anisotropy, the rate constants depend on the surface orientation with respect to the crystal, as well as on the local electric field  $F$  at the surface:

$$k_x = k_x^0(\mathbf{n}, F, \beta) \exp[-\beta E_x(\mathbf{n}, F)], \quad (7)$$

if we denote the unit vector normal to the surface as

$$\mathbf{n} = (\xi, \eta, \zeta) = \frac{(h, k, l)}{\sqrt{h^2 + k^2 + l^2}}, \quad (8)$$

in terms of Miller's indices ( $hkl$ ). To represent the anisotropy of the fcc crystal, the activation energies can be expanded into the so-called cubic harmonics [41] as

$$E_x(\xi, \eta, \zeta) = E_x^{(0)} + E_x^{(4)} (\xi^4 + \eta^4 + \zeta^4) + E_x^{(6)} \xi^2 \eta^2 \zeta^2 + \dots \quad (9)$$

Moreover, the dependence on the electric field can be expressed as

$$E_x(F) = E_x(0) - d_x F - \frac{1}{2} \alpha_x F^2 + \dots \quad (10)$$

to describe the possible effects of an effective dipole  $d_x$ , an effective polarizability  $\alpha_x$ , or higher nonlinear terms [42].

Besides, the activation energies may also depend on the local coverages if lateral interactions manifest themselves, as explained here below.

The parameters defining the rate constants of the present model are given in Table II. The determination of these parameters is explained here below in Subsections IV B-IV E. Although many values remain the same as in our previous work based on the deterministic mean-field kinetic equations [34–36], some parameters had to be adapted to the present stochastic model, specifically,  $A_K^S(011) +4\%$ ,  $A_K^S(111) +4\%$ ,  $k_{\text{ox}}^0 \times 1.8$ ,  $k_{\text{red}}^0 \times 1.6$ ,  $E_{\text{red}}(001) +1\%$ ,  $E_{\text{red}}(011) +5\%$ ,  $E_{\text{red}}(111) +6\%$ ,  $A_{\text{red}}^S -13\%$ ,  $k_r^0 \times 1.1$ ,  $E_r(001) +1\%$ ,  $E_r(011) +1\%$ ,  $E_r(111) -7\%$ ,  $A_r^O -17\%$ , and  $A_r^H +33\%$ . These changes are needed in order to reproduce the experimental observations in the oscillatory and bistable regimes (see below).

Hydrogen adsorption	Hydrogen desorption
$S_{\text{H}}^0 = 0.3$	$k_{\text{dH}}^0 = 3 \times 10^{10} \text{ s}^{-1}$ $E_{\text{dH}}(001) = 0.75 \text{ eV}$ $E_{\text{dH}}(011) = 0.64 \text{ eV}$ $E_{\text{dH}}(111) = 0.70 \text{ eV}$ $d_{\text{dH}} = 0.005 \text{ eV nm V}^{-1}$
Oxygen adsorption	Oxygen desorption
$S_{\text{O}}^0(001) = 0.95$ $S_{\text{O}}^0(011) = 0.95$ $S_{\text{O}}^0(111) = 0.60$ $E_{\text{K}} = -0.178 \text{ eV}$ $K^0 = 0.2525 \text{ eV}$ $A_{\text{K}}^{\text{O}} = 0.158 \text{ eV}$ $A_{\text{K}}^{\text{S}}(001) = 0.070 \text{ eV}$ $A_{\text{K}}^{\text{S}}(011) = 0.078 \text{ eV}$ $A_{\text{K}}^{\text{S}}(111) = 0.085 \text{ eV}$	$k_{\text{d}}^0 = 6 \times 10^{13} \text{ s}^{-1}$ $E_{\text{d}}(001) = 3.50 \text{ eV}$ $E_{\text{d}}(011) = 3.20 \text{ eV}$ $E_{\text{d}}(111) = 2.85 \text{ eV}$ $A_{\text{d}}(001) = -0.60 \text{ eV}$ $A_{\text{d}}(011) = -0.50 \text{ eV}$ $A_{\text{d}}(111) = -0.40 \text{ eV}$ $B_{\text{d}}(001) = -0.80 \text{ eV}$ $B_{\text{d}}(011) = -0.70 \text{ eV}$ $B_{\text{d}}(111) = -0.50 \text{ eV}$
Oxidation	Reduction
$k_{\text{ox}}^0 = 9 \times 10^{11} \text{ s}^{-1}$ $E_{\text{ox}}(001) = 1.52 \text{ eV}$ $E_{\text{ox}}(011) = 1.63 \text{ eV}$ $E_{\text{ox}}(111) = 1.68 \text{ eV}$ $d_{\text{ox}}(001) = 0.035 \text{ eV nm V}^{-1}$ $d_{\text{ox}}(011) = 0.025 \text{ eV nm V}^{-1}$ $d_{\text{ox}}(111) = 0.020 \text{ eV nm V}^{-1}$	$k_{\text{red}}^0 = 3 \times 10^{13} \text{ s}^{-1}$ $E_{\text{red}}(001) = 1.48 \text{ eV}$ $E_{\text{red}}(011) = 1.65 \text{ eV}$ $E_{\text{red}}(111) = 1.68 \text{ eV}$ $d_{\text{red}}(001) = 0.0200 \text{ eV nm V}^{-1}$ $d_{\text{red}}(011) = 0.0175 \text{ eV nm V}^{-1}$ $d_{\text{red}}(111) = 0.0150 \text{ eV nm V}^{-1}$ $A_{\text{red}}^{\text{S}} = 0.26 \text{ eV}$
Water formation	
$k_{\text{r}}^0 = 8 \times 10^{12} \text{ s}^{-1}$ $E_{\text{r}}(001) = 0.80 \text{ eV}$ $E_{\text{r}}(011) = 0.80 \text{ eV}$ $E_{\text{r}}(111) = 0.70 \text{ eV}$	$d_{\text{r}} = -0.0075 \text{ eV nm V}^{-1}$ $A_{\text{r}}^{\text{O}} = -0.170 \text{ eV}$ $A_{\text{r}}^{\text{H}} = -0.180 \text{ eV}$

TABLE II: Table of the parameters used in the present model for hydrogen and oxygen on rhodium.

### B. Hydrogen adsorption and desorption

The adsorption of hydrogen is dissociative:



The adsorption rate constant is given by

$$k_{\text{aH}} = \frac{S_{\text{H}}^0 a_s}{\sqrt{2\pi m_{\text{H}_2} k_{\text{B}} T}} \quad (12)$$

with  $m_{\text{H}_2} = 2.016 \text{ amu}$  and the reference unit area  $a_s = 10 \text{ \AA}^2$  taken independently of the orientation [35]. The sticking coefficient  $S_{\text{H}}^0$  takes the same value for all the orientations according to the experimental value at zero coverage reported in Ref. [43].

On the other hand, the desorption rate constant is given by

$$k_{\text{dH}} = k_{\text{dH}}^0 e^{-\beta(E_{\text{dH}} - Fd_{\text{dH}})}, \quad (13)$$

where the desorption energy  $E_{\text{dH}}$  depends on the surface orientation. The parameters  $k_{\text{dH}}^0$  and  $E_{\text{dH}}$  given in Table II have been fitted to temperature-programmed desorption (TPD) spectra [36]. These spectra have been simulated and

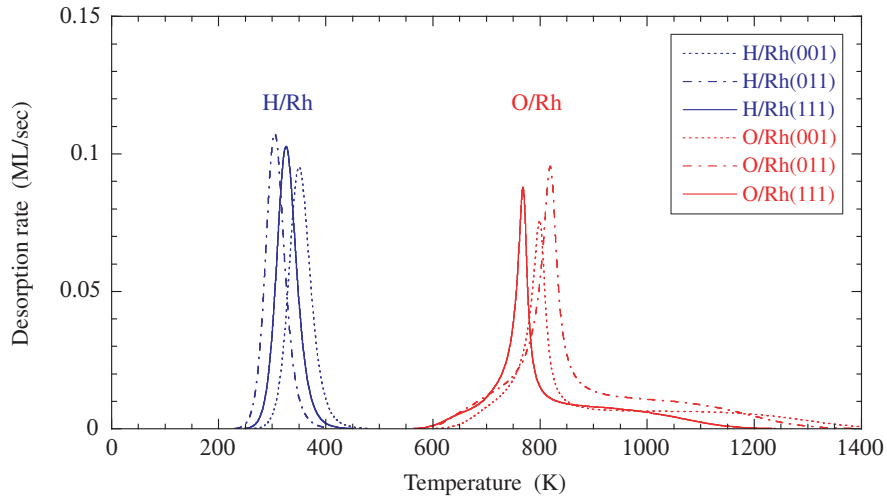


FIG. 6: TPD spectra of hydrogen and oxygen on Rh(001) (dashed line), Rh(011) (long-short dashed line), and Rh(111) (solid line) numerically simulated with the present kinetic model. The temperature ramp is  $T = T_0 + \gamma t$  with  $\gamma = 10$  K/s,  $T_0 = 100$  K for hydrogen, and  $T_0 = 500$  K for oxygen. The initial coverage is  $\theta_H(0) = 0.5$  ML for hydrogen and  $\theta_O(0) = \theta_s(0) = 1$  ML for oxygen, which corresponds to the surface oxide trilayer O(ad)-Rh-O(sub).

are depicted for the present model in Fig. 6, showing agreement with known TPD spectra [43–45]. The value of  $d_{dH}$  was chosen to be consistent with the results of DFT calculations, showing that the hydrogen binding energy decreases with a positive electric field [35].

The desorption energies for hydrogen are small compared to those of oxygen, so that the hydrogen coverage of the surface is small in the temperature range  $400 \text{ K} < T < 600 \text{ K}$  of the experiment, as observed on the TPD spectra of Fig. 6.

### C. Oxygen adsorption and desorption

The adsorption of oxygen is also dissociative and proceeds via a precursor state:



Accordingly, the overall equation reads



with the effective adsorption and desorption rate constants:

$$k_{aO} = \frac{\tilde{k}_a K}{1 + K \theta_\emptyset^2}, \quad (17)$$

$$k_{dO} = \frac{k_d}{1 + K \theta_\emptyset^2}, \quad (18)$$

where  $\theta_\emptyset = 1 - \theta_H - \theta_O$  and

$$K = \frac{k_a}{\tilde{k}_d} = K^0 e^{-\beta(E_K + A_K^O \theta_O + A_K^S \theta_S)}. \quad (19)$$

The prefactor  $K^0$ , the activation barrier  $E_K$ , and the mean-field oxygen coverage dependence  $A_K^O$  were fitted to the experimental sticking coefficient of Ref. [46]. Besides, the dependence of the constant (19) on the presence of

subsurface oxygen by the parameter  $A_K^S$  describes the inhibition of oxygen adsorption due to the formation of an oxide layer. This inhibition is at the origin of oscillatory behavior in the dynamics of this model [34–36].

The adsorption rate of the precursor is given by

$$\tilde{k}_a = \frac{S_O^0 a_s}{\sqrt{2\pi m_{O_2} k_B T}} \quad (20)$$

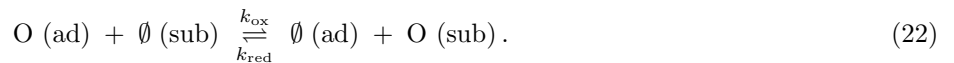
with  $m_{O_2} = 31.99$  amu, the same reference unit area  $a_s = 10 \text{ \AA}^2$  as above, and the sticking coefficient  $S_O^0$  with an assumed structure dependence [35]. The desorption rate

$$k_d = k_d^0 e^{-\beta(E_d - d_a F + A_d \theta_O + B_d \theta_O^2)} \quad (21)$$

has been fitted in Refs. [34–36] to TPD spectra [47–49], giving the parameter values of Table II. In the constants (19) and (21), the activation energies are influenced by lateral interactions between neighboring oxygen atoms, leading in particular to the broad TPD spectra for oxygen in Fig. 6.

#### D. Surface oxide formation

Adsorbed oxygen may go subsurface to form a surface oxide trilayer O(ad)-Rh-O(sub), which has been studied in detail [50–54]. The formation of this surface oxide is described by the oxidation of Rh due to the subsurface transfer of oxygen and the reverse reaction of reduction:



The rates of oxidation and reduction are given by

$$k_{\text{ox}} = k_{\text{ox}}^0 e^{-\beta(E_{\text{ox}} - d_{\text{ox}} F)}, \quad (23)$$

$$k_{\text{red}} = k_{\text{red}}^0 e^{-\beta(E_{\text{red}} - d_{\text{red}} F + A_{\text{red}}^S \theta_S)}, \quad (24)$$

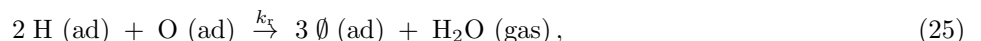
with the parameters of Table II.

If the surface is at equilibrium with gaseous oxygen, a phase transition is known to happen from the metallic state to the surface oxide at critical values of dioxygen pressure that are specific for the different surface orientations (001), (011), and (111) [50–54]. The parameters defining the rates (23) and (24) have been fitted to reproduce this transition at the known values of the critical dioxygen pressure [34–36]. Moreover, the parameters  $d_{\text{ox}}$  and  $d_{\text{red}}$  fixing the dependence of the rates (23)-(24) on the electric field has been obtained by DFT calculations [55]. Since oxygen is more electronegative than rhodium, the electric field facilitates the formation of the surface oxide. In this respect, the effective dipolar moment is larger for oxidation than reduction,  $d_{\text{ox}} > d_{\text{red}}$ , as shown in Table II. Accordingly, the field promotes the oxidation of the rhodium tip [55].

TPD spectra simulated for oxygen with the parameter values of Table II are shown in Fig. 6 and they are in agreement with experimental spectra [36]. As seen in Fig. 6, oxygen remains strongly bounded to the rhodium surface in the temperature range  $400 \text{ K} < T < 600 \text{ K}$  of the experiment.

#### E. Reaction of water formation

As discussed elsewhere [34–36], the bottleneck for water formation is the addition of the first hydrogen. The addition of the second hydrogen is fast so that the lifetime of OH(ad) is relatively short. Accordingly, the reaction of water formation reads



where the rate constant depends on hydrogen and oxygen coverages in order to reproduce the experimentally observed bistability and oscillations:

$$k_r = k_r^0 e^{-\beta(E_r - d_r F + A_r^H \theta_H + A_r^O \theta_O)} \quad (26)$$

with the parameters given in Table II. The dependence of this rate constant on the electric field is such that the activation barrier in the formation of water is increased by a positive electric field, which is also the case in other

systems [56]. Here, the activation energy is taken to depend linearly on the electric field, but nonlinear dependences could be considered as in Eq. (10). Besides, the parameters  $A_r^H$  and  $A_r^O$  describe the interaction between oxygen and hydrogen, which manifests itself in TPD spectra when these species are coadsorbed on rhodium [57]. The parameters in the rate constant (26) have values that have been modified with respect to those of Refs. [34–36] in order to reproduce quantitatively the conditions of oscillations in the present stochastic model, as discussed in Section VII.

The reaction is supposed to be fully irreversible with a vanishing water pressure  $P_{H_2O} = 0$  around the rhodium tip.

## V. SURFACE TRANSPORT

### A. Ultrafast hydrogen diffusion on metallic surfaces

Adsorbed hydrogen is known to have an ultrafast diffusion on metallic surfaces with a diffusion coefficient given by  $D_H = D_H^0 \exp(-\beta E_{\text{diff,H}})$  with a very small activation energy  $E_{\text{diff,H}} = 0.187$  eV and  $D_H^0 \simeq 10^{-3}$  cm<sup>2</sup>/s [58, 59]. Accordingly, at the temperature of 450 K, the diffusion time over a distance of the order of the radius of curvature  $R = 19$  nm is equal to  $t_{\text{diff,H}} = R^2/D_H = 4.5 \times 10^{-7}$  s, which is seven orders of magnitude shorter than the time scale of observed phenomena. As a consequence, hydrogen adatoms would quickly relax towards a quasi-equilibrium distribution in the metallic regions.

In our previous work [34–36], we assumed that this ultrafast diffusion holds globally on the surface of the tip depending on the availability of empty sites by taking  $D_H = D_H^0 \exp(-\beta E_{\text{diff,H}}) \times (1 - \theta_O)$ . The convention of Refs. [30, 60, 61] is here adopted for the diffusion coefficient  $D_H$ , so that the diffusive flux of hydrogen is in principle given by

$$\mathbf{J}_H = -L_H \nabla(\beta\mu_H) \quad (27)$$

with the Onsager coefficient

$$L_H = D_H \frac{\theta_H(1 - \theta_H - \theta_O)}{1 - \theta_O} \quad (28)$$

and the chemical potential

$$\mu_H = U_H + \beta^{-1} \ln \frac{\theta_H}{1 - \theta_H - \theta_O} \quad (29)$$

where  $U_H$  is the potential energy of hydrogen. We notice that the previously chosen dependence of the diffusion coefficient on the oxygen coverage  $\theta_O$  does not change the order of magnitude of hydrogen diffusion, unless the oxygen coverage is very nearly equal to unity, so that a global ultrafast diffusion was assumed in Refs. [34–36]. However, stochastic simulations with this assumption could not reproduce the random switches of the quadrants, as observed in the experiment. Therefore, the assumption of global ultrafast diffusion has been revisited by considering the possibility of mechanisms blocking hydrogen diffusion in the regions sufficiently covered by oxygen.

### B. Hydrogen diffusion with percolation and lateral interactions

At least two mechanisms can block hydrogen diffusion in the presence of oxygen on the surface.

The first mechanism is percolation [61–63], which can be introduced as follows. If the surface is randomly covered by oxygen adatoms, they constitute so many obstacles to the surface diffusion of hydrogen adatoms. Percolation is the formation of an infinite cluster of sites left vacant by oxygen, allowing the transport of hydrogen across the whole surface. No such infinite cluster exists if oxygen is too densely covering the surface, i.e., if the sites are void of oxygen with a too low probability  $p$ . The percolation of an infinite cluster of sites unoccupied by oxygen becomes possible if the probability  $p$  exceeds a critical threshold, which is equal to  $p_c \simeq 0.592746$  for a square lattice, and  $p_c = 0.5$  for a triangular lattice. In finite-size systems, the threshold takes an effective value  $p_c$  that is smaller than for infinite lattices [62, 63]. In the present system, the percolation threshold corresponds to the oxygen coverage  $\theta_{O,c} = 1 - p_c$ . Hydrogen can diffuse over the whole surface only if the oxygen coverage is lower than  $\theta_{O,c}$ .

A second and related mechanism is due to the lateral interactions of the oxygen adatoms, which locally modify the potential energy surface of the hydrogen adatoms. The potential energy surface is not only repulsive at the sites occupied by oxygen adatoms, but barriers may also be generated on the neighboring sites so that the potential energy surface becomes highly dependent on the locations of oxygen adatoms [30, 61]. Moreover, the reaction of OH formation is favored, which also affects or stops hydrogen diffusion.

These mechanisms suggest that hydrogen diffusion is limited in the cross-like zone covered by oxygen and separating the four quadrants in Fig. 2. The presence of this cross-like barrier to hydrogen diffusion can explain that the four quadrants randomly switch independently of each other, as shown by the simulations detailed here below.

To take into account these mechanisms, we assume that the diffusion coefficient is effectively given by

$$D_H = D_H^0 e^{-\beta(E_{\text{diff,H}} + A_{\text{diff,H}}\theta_O + B_{\text{diff,H}}\theta_O^2)} (1 - \theta_O). \quad (30)$$

This expression accounts for the partial confinement of hydrogen by oxygen through an exclusion factor  $1 - \theta_O$  and for lateral interactions characterized by the parameters  $A_{\text{diff,H}} = 1.25$  eV and  $B_{\text{diff,H}} = -0.89$  eV, chosen to significantly reduce diffusion at oxygen coverages  $\theta_O > 0.4$ , as depicted in Fig. 7.

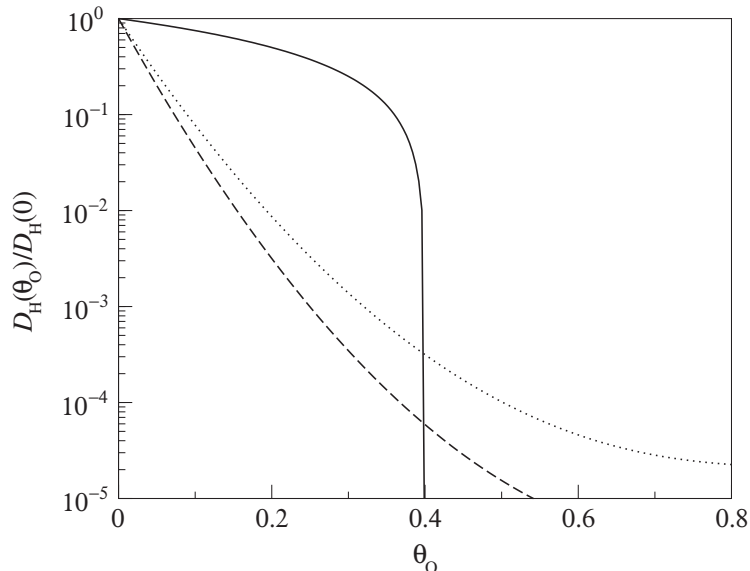


FIG. 7: Semi-logarithmic plot of the effective diffusion coefficient of hydrogen as a function of the oxygen coverage  $\theta_O$  for  $T = 450$  K (dashed line) and  $T = 550$  K (dotted line). These curves correspond to Eq. (30) with  $E_{\text{diff,H}} = 0.187$  eV,  $A_{\text{diff,H}} = 1.25$  eV, and  $B_{\text{diff,H}} = -0.89$  eV. The full line is the effective medium approximation of percolation theory [64, 65]:  $D_H(\theta_O) = D_H(0) (\theta_c - \theta_O)/\theta_c$  for  $\theta_O < \theta_c$  with  $\theta_c \simeq 0.4$ , which is shown for comparison.

Accordingly, hydrogen diffusion is assumed to be negligible if  $D_H(\theta_O)/D_H(0) < 10^{-4}$ , which happens when the oxygen coverage is above a threshold value  $\theta_{O,c}$  that depends on temperature, as seen in Fig. 7. The value  $\theta_{O,c}$  increases with temperature. Moreover, hydrogen transport is supposed to be ultrafast in the domains where the local oxygen coverage is below the threshold value  $\theta_O < \theta_{O,c}$ . Consequently, regarding hydrogen diffusion, the grid facets where  $\theta_O < \theta_{O,c}$  are grouped into percolation clusters. Figure 8 illustrates the formation of percolation clusters that would result from a purely random distribution of obstacles with a uniform coverage  $\theta_O = 0.43$  on the surface. The clustering is carried out at the level of the sites in Fig. 8a, and at the level of the facets in Fig. 8b using the mean facet coverage of the configuration shown in Fig. 8a. In Fig. 8b, each cluster  $j$  is composed of a set  $\{i\}_{i=1}^{n_j}$  of  $n_j$  facets. This example is hypothetical because the coverage is nonuniform in general due to the anisotropy of the underlying crystal and the spatially varying electric field.

### C. Quasi-equilibrium hydrogen distribution in each percolation cluster

Now, we may assume that, in each cluster  $j$ , hydrogen reaches a quasi-equilibrium canonical distribution by the ultrafast transport of hydrogen adatoms among the facets  $\{i\}_{i=1}^{n_j}$  composing the cluster  $j$ . If the hydrogen population is small, it takes the form of the following multinomial distribution for each cluster

$$P_c(\{H_i\}) \simeq \frac{1}{Z(H_j)} \prod_{i=1}^{n_j} \frac{1}{H_i!} [(N_i - O_i) e^{-\beta U_{H_i}}]^{H_i}, \quad (31)$$

where  $\{H_i\}_{i=1}^{n_j}$  are the hydrogen populations on the facets  $\{i\}_{i=1}^{n_j}$  of the cluster  $j$ ,  $H_j = \sum_{i=1}^{n_j} H_i$  is the total number of hydrogen adatoms in the cluster  $j$ ,  $Z(H_j)$  is the corresponding partition function, and  $U_{H_i}$  is the potential energy

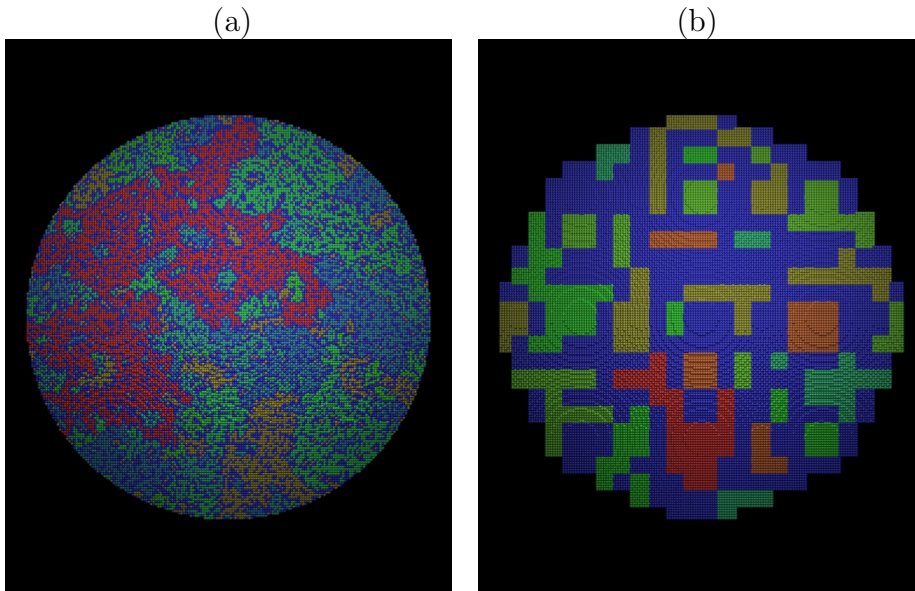


FIG. 8: (a) Vacant site percolation clusters on the tip surface. Dark (blue) sites are uniformly occupied by obstacles with the coverage  $\theta_O = 0.43$ . Nearest-neighboring vacant sites are connected and form clusters of varying sizes and geometries shown with different colors. (b) Facet percolation clusters constructed from the configuration shown in (a). On the dark (blue) facets, the mean coverage is  $\theta_O > 0.43$ . Nearest-neighboring facets with  $\theta_O < 0.43$  are connected, resulting in clusters shown with different colors chosen to make the distinction between them.

of a hydrogen adatom bound to the facet  $i$ , as shown in Appendix A. In order to achieve a global thermodynamic equilibrium with the gas phase in the electric field  $F$ , the potential energy is taken equal to

$$U_H = -\frac{1}{2} \left( E_{dH} - d_{dH}F + \frac{1}{2} \alpha_{H_2} F^2 \right) + \text{cst}, \quad (32)$$

as shown elsewhere [34–36]. This potential energy locally varies from facet to facet with the electric field (3) and the hydrogen desorption energy  $E_{dH}$  according to Table II. We notice that the hydrogen adatoms move in the highly nonuniform potential (32), so that their diffusion is biased and combined with the drift induced by the force,  $\mathbf{f} = -\nabla U_H$ , which is tangent to the surface [66].

Since oxygen evolves in time due to the different kinetic processes, facet clustering should be adapted accordingly. Therefore, between each update of the surface coverage by the adsorption-desorption-reaction random events (see Section VI), the ultrafast hydrogen transport is carried out by first constructing the percolation clusters of facets according to the oxygen coverage, and secondly performing in each cluster a redistribution of the hydrogen adatoms among all the facets  $\{i\}_{i=1}^{n_j}$  currently composing every cluster  $j$ , and this for all the clusters.

## VI. STOCHASTIC ALGORITHM

The stochastic algorithm numerically simulates the random time evolution of the numbers  $\{H_i, O_i, S_i\}_{i=1}^n$  of the different species in all the grid facets  $\{i\}_{i=1}^n$  covering the tip, as shown in Fig. 5b. These numbers evolve due to random events of hydrogen and oxygen adsorption, hydrogen desorption, rhodium oxidation and reduction, water formation (which are local in every facet), and hydrogen diffusion between the facets. Accordingly, at each time step, the adsorption-desorption-reaction (adr) updates can be performed in parallel in every facet, while hydrogen redistribution in the percolation clusters can follow to start again at the next time step.

In order to describe the algorithm, we consider the master equation for the time evolution of the joint probability  $P_t(\{H_i, O_i, S_i\})$  to find the facets with  $\{H_i\}$  hydrogen adatoms,  $\{O_i\}$  oxygen adatoms, and  $\{S_i\}$  subsurface oxygen atoms at time  $t$ :

$$\frac{d}{dt} P_t = \left( \hat{L}_{\text{adr}} + \hat{L}_{\text{diff}} \right) P_t, \quad (33)$$

where  $\hat{L}_{\text{adr}} = \sum_{i=1}^n \hat{L}_{\text{adr},i}$  denotes the terms describing the updates due to adsorption, desorption, and reaction, while  $\hat{L}_{\text{diff}}$  represents the algorithm of hydrogen redistribution described in the previous Section V.

*A priori*, Gillespie's algorithm could be chosen to simulate adsorption, desorption, and reaction [67, 68]. However, the time steps of this algorithm are varying from step to step. Since we need to alternate diffusion with adsorption, desorption, and reaction, an equal time step  $\Delta t$  should be adopted. The time step is small enough, the time evolution could thus proceed according to

$$P_{t+\Delta t} \simeq \exp\left(\hat{L}_{\text{diff}}\Delta t\right) \prod_{i=1}^n \exp\left(\hat{L}_{\text{adr},i}\Delta t\right) P_t, \quad (34)$$

by performing hydrogen redistribution between the facets after the updates due to adsorption, desorption, and reaction in every facet  $\{i\}$ .

A special algorithm has been used in order to simulate adsorption, desorption, and reaction, which is described in Appendix B. In summary, the numbers  $H_i$ ,  $O_i$ , and  $S_i$  are updated to new values taken as multinomial random variables. The algorithm corresponds to the linearization of the mean-field kinetic equations, so that the time step  $\Delta t$  should take a sufficiently small value. The algorithm is exact for linear reactions and it offers the advantage that the time step can be chosen equal in the whole simulation, while preserving the non-negativity of the variables  $\{H_i, O_i, S_i\}$  even if these numbers are close to zero. The multinomial random variables are taken in order to satisfy the master equation of adsorption, desorption, and reaction in the limit  $\Delta t \rightarrow 0$ . The details of the algorithm are given in Appendix B. The results presented below are obtained with simulations where the time step is taken equal to  $\Delta t = 2 \times 10^{-6}$  s.

## VII. RESULTS ON THE OSCILLATORY REGIME

The oscillations observed in the experiment around 550 K are reproduced with the present stochastic model, as well as with the previous deterministic mean-field model [34–36]. For the stochastic model, several parameters had to be readjusted to reproduce the experimental observations. These parameters are those controlling the dynamical aspects, which include the parameter  $A_K^S$  describing the inhibition of oxygen adsorption by subsurface oxygen in Eq. (19), the parameters of the oxidation and reduction rates (23) and (24), as well as the reaction rate constant (26). The oscillations simulated by the stochastic process have thus the same features as for the mean-field kinetic model. At the temperature of 550 K, the percolation threshold  $\theta_{O,c}$  is too high to be reached during the process so that a single large percolation cluster remains formed over the whole surface. Accordingly, hydrogen diffusion is ultrafast and global on the surface in this regime, as assumed in our previous work [34–36].

As shown in Fig. 9, the surface oscillates between a metallic state with a low oxygen occupation to an oxidized state with a high occupation by adsorbed and subsurface oxygen. At the end of this cycle when oxygen occupation is still high, adsorbed oxygen is consumed by water formation more quickly than subsurface oxygen, as seen in Fig. 9. This surface state with a lot of subsurface oxygen but a small amount of adsorbed oxygen is very unstable and a sudden reduction of the surface happens, leading to the recovery of the metallic state with a low oxygen occupation. Although hydrogen coverage is always very small at 550 K as expected from the TPD spectra of Fig. 6, it is larger on the metallic surface than on the oxidized one. Since the oxygen coverage is always larger, the rate  $k_r\theta_H\theta_O$  of water formation is higher on the metallic surface. Therefore, the brightness of the surface, which is determined by the ionized fraction of water, is higher for the metallic than the oxidized surface, which explains the observations [34–36]. The cycle starts again from the metallic state with the formation of the surface oxide at the topmost (001) facet of the tip. The oxide layer anisotropically expands first along the  $\{011\}$  zone lines and, thereafter, over the whole tip, including the  $\{111\}$  facets.

The time evolution of the average hydrogen, oxygen, and subsurface oxygen occupations on a tip with a radius of curvature equal to 19 nm is depicted as the solid lines in Fig. 9a. The dashed lines show the influence of noise on the time dependence. The noise amplitude can be varied by changing the numbers of sites  $\{N_i\}$  on the facets. The deterministic time evolution is reached in the limit where these numbers take arbitrarily large values  $N_i \rightarrow \infty$ . In Fig. 9a, a stochastic simulation with the site numbers of Table I for the radius 19 nm (solid lines) is compared with another one with  $10^3$  times larger numbers, in which noise is thus smaller (dashed lines). Indeed, we observe in Fig. 9a that noise affects more strongly the solid than the dashed lines. Moreover, the period tends to increase as the noise amplitude decreases.

The results of the stochastic simulation with a reduced noise amplitude are compared with those of the deterministic kinetic model in Fig. 9b, which depicts the hydrogen, oxygen, and subsurface oxygen occupations on the (001) facet. This facet is located at the apex of the tip where the electric field is the highest. As aforementioned, the oxide layer is most prominent at the apex. Indeed, the subsurface oxygen occupation nearly reaches the unit value,  $\theta_S = 1$

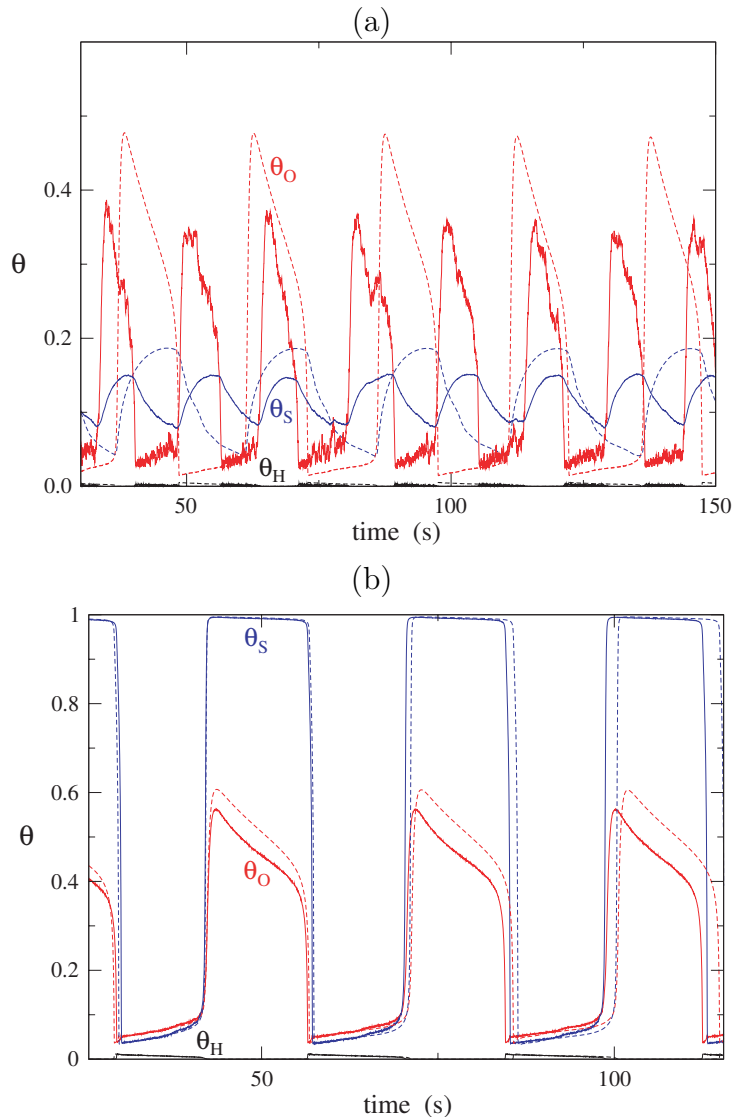


FIG. 9: Time evolution of the hydrogen, oxygen, and subsurface oxygen occupations in the oscillatory regime at 550 K,  $P_{O_2} = 2 \times 10^{-3}$  Pa,  $P_{H_2} = 3.8 \times 10^{-3}$  Pa, and  $F_0 = 12$  V/nm: (a) The occupations averaged over the whole surface. The solid lines are the results of stochastic simulations for a tip with radius 19 nm, and the dashed lines for a system containing  $10^3$  times more sites. The lower curves are for the hydrogen coverages  $\theta_H$ , the intermediate curves for the subsurface oxygen coverages  $\theta_S$ , and the upper curves for the oxygen coverages  $\theta_O$ . (b) The occupations on the (001) facet. The deterministic kinetic model (dashed lines) is compared with stochastic simulations (solid lines) in the limit of a large system (the number of sites is  $10^3$  times that of a tip with a 19 nm radius). The lower curves are for the hydrogen coverages  $\theta_H$ , the intermediate curves for the oxygen coverages  $\theta_O$ , and the upper curves for the subsurface oxygen coverages  $\theta_S$ .

when the surface is oxidized, as seen in Fig. 9b. In this regard, we notice that the subsurface oxygen occupation is significantly lower in Fig. 9a because of the averaging over the whole surface, which includes areas remaining metallic during longer lapses of time. Figure 9b shows that the stochastic process with site numbers  $10^3$  times larger than in Table I has essentially the same time evolution as the deterministic kinetic model, which confirms the consistency of the stochastic modeling.

Since the oscillations continue to exist in the deterministic limit, they do not constitute a phenomenon requiring the stochastic approach to be understood, in contrast to the burst noise observed in the bistable regime, to which the next Section VIII is devoted.

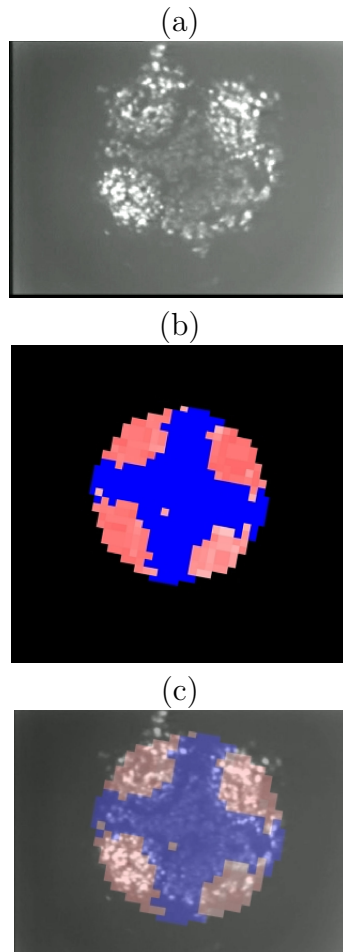


FIG. 10: (a) FIM micrograph of the rhodium tip showing the spatial extension of the hydrogen-covered quadrants with the oxidized cross-like zone in the bistable regime at 450 K,  $P_{\text{O}_2} = 5.0 \times 10^{-4}$  Pa,  $P_{\text{H}_2}/P_{\text{O}_2} = 10.0$ , and  $F_0 = 12.3$  V/nm (same experimental conditions as in Fig. 2). (b) Spatial extension of a corresponding state obtained by stochastic simulation for 450 K,  $P_{\text{O}_2} = 5.0 \times 10^{-4}$  Pa,  $P_{\text{H}_2} = 9.0 \times 10^{-4}$  Pa,  $F_0 = 12.3$  V/nm, and  $R = 19$  nm (same conditions as in Fig. 13). (c) Superposition of image (a) and (b) for comparison.

## VIII. RESULTS ON THE REGIME OF BISTABILITY

In this section, the results on the bistability extending over the temperature range  $400 \text{ K} < T < 525 \text{ K}$  are reported.

### A. Spatial structure

The stochastic model is able to explain the spatial structures observed in the experiment, especially, the formation of the cross-like zone where the rhodium surface is oxidized. The mechanisms at play in the formation of this structure are the anisotropy of the underlying fcc crystal and the electric field, which both modulate the rates on the surface. On the one hand, the parameters determining the rates depend on the surface orientation of the facets, as shown in Table II. On the other hand, the formation of the surface oxide is facilitated by the electric field, which is larger at the apex than in the flanks.

The combination of these mechanisms generates the pattern shown in Fig. 10 comparing the experimental observation with a simulation of the stochastic model. The four quadrants including the facets  $\{111\}$  are metallic and slightly covered by hydrogen. These quadrants correspond to several percolation clusters where hydrogen adatoms undergo rapid transport by diffusion in the potential (32). The percolation clusters are formed because the temperature is now lower than in the oscillatory regime, whereupon the percolation threshold takes the smaller value  $\theta_{\text{O},c} \simeq 0.4$  and this

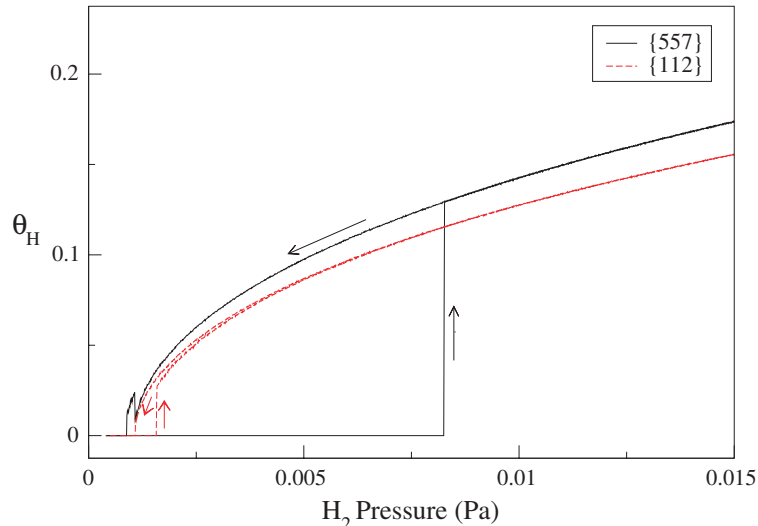


FIG. 11: Hysteresis in the hydrogen coverage  $\theta_H$  on the facets  $\{557\}$  (full line) and the facets  $\{112\}$  (dashed line) upon cyclic variation of the hydrogen pressure for 450 K,  $P_{O_2} = 5.0 \times 10^{-4}$  Pa,  $F_0 = 12.3$  V/nm, and  $R = 19$  nm. As seen in Fig. 16b, the facets  $\{557\}$  are nearby the facets  $\{111\}$  in the middle of the quadrants and the facets  $\{112\}$  are closer to the apex (001).

oxygen coverage is reached in the bistable regime. The four quadrants are separated by the cross-like zone including the apex (001) and the facets  $\{011\}$ . In this zone, the surface is covered by the oxide trilayer O(ad)-Rh-O(sub), so that the hydrogen coverage is vanishing. Since the FIM signal is due to water cations and the rate of water formation is proportional to  $k_r \theta_H \theta_O$ , the hydrogen-covered quadrants are brighter than the oxidized cross-like zone, as seen in Fig. 10, which is reminiscent of the structure already investigated in our previous work [34–36].

### B. Hysteresis

The phenomenon of hysteresis is generated by varying up and down the hydrogen pressure, as depicted in Fig. 11 on two sets of facets along the diagonal line across the quadrants. The hydrogen pressure is increased (respectively decreased) by steps of  $\Delta P_{H_2} = 10^{-5}$  Pa every  $\Delta t = 2$  s in the range extending between  $P_{H_2} = 4 \times 10^{-4}$  Pa and  $P_{H_2} = 2 \times 10^{-2}$  Pa. As the hydrogen pressure is increased, the oxygen coverage suddenly drops to a small value when the hydrogen coverage jumps to its upper value, which reveals the bistability. Thereafter, the hydrogen coverage remains on the upper branch of bistability as the hydrogen pressure is decreased down to its value where the surface again becomes covered by oxygen. For the whole surface, the hysteretic loop extends from the largest hydrogen pressure, at which all the facets go back to the oxygen-covered state, up to the smallest hydrogen pressure, at which all the facets are covered by hydrogen.

### C. Bistability diagram

The hydrogen pressure is increased and decreased as aforementioned for different values of the temperature in order to obtain the bistability diagrams of Fig. 12 in comparison with experimental data. As in Fig. 11, the hydrogen pressure is increased (respectively decreased) by steps of  $\Delta P_{H_2} = 10^{-5}$  Pa every  $\Delta t = 2$  s, while going upward (respectively downward) at each value of the temperature.

The domain of bistability extends between the upper curve where the metallic surface is recovered when the hydrogen pressure is high enough, and the lower curve where the surface becomes oxidized again when the hydrogen pressure is too low. Since the process is stochastic, the transitions between both surface states may happen at different values of the hydrogen pressure depending on the run. Consequently, averages over 8 runs have been performed for each value of the temperature in order to obtain Fig. 12 where the black circles are the experimental data and the open circles the results of the simulations. The error bars depicted in Fig. 12 are determined using the 8 runs, which shows that the transition at high pressure from the oxidizing to the metallic surface is more affected by stochasticity than the transition at low pressure back to the oxidized surface.

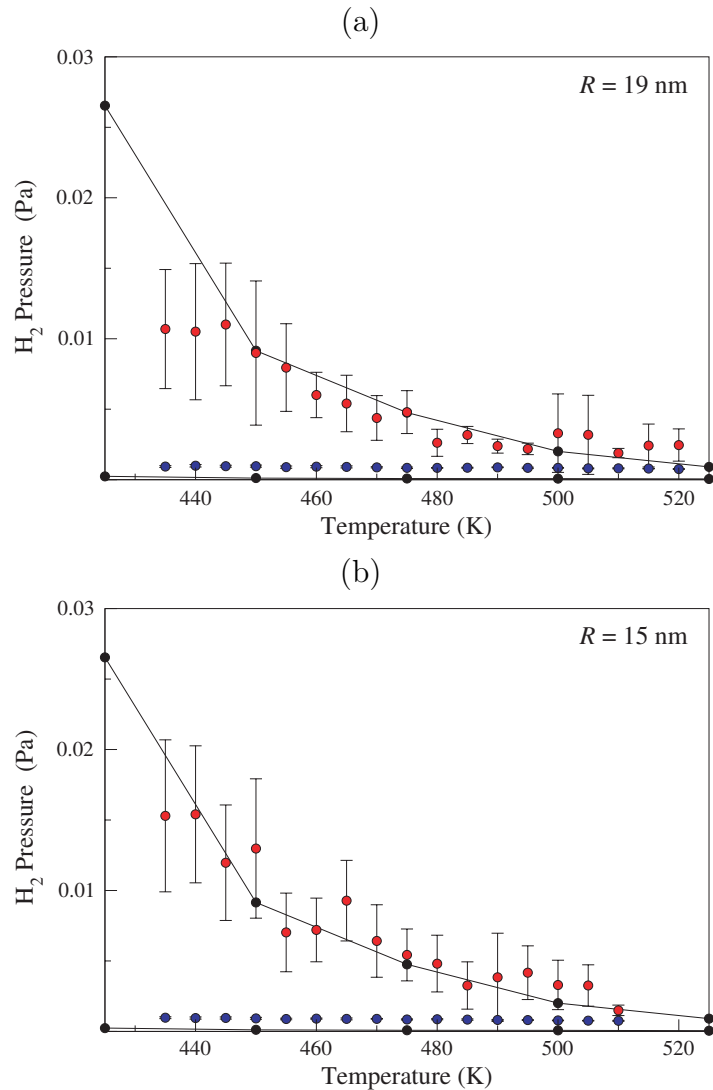


FIG. 12: Bistability diagram constructed from the hysteresis curves shown in Fig. 11 for tip radius (a) 19 nm and (b) 15 nm with  $P_{\text{O}_2} = 5.0 \times 10^{-4}$  Pa and  $F_0 = 12.3$  V/nm. The black circles connected by a line are the experimental pressures for which changes in the surface composition occur when increasing (upper curve) and decreasing (lower curve) the hydrogen pressure. The circles with error bars are the pressures obtained by stochastic simulations at 450 K,  $P_{\text{O}_2} = 5.0 \times 10^{-4}$  Pa, and  $F_0 = 12.3$  V/nm. In the simulations, the hydrogen pressure is increased (resp. decreased) by steps of  $\Delta P_{\text{H}_2} = 10^{-5}$  Pa every  $\Delta t = 2$  s, while going upward (resp. downward) along the hysteretic cycle. The area between the curves marks the region of bistability. The average values and error bars are obtained with 8 runs at every value of the temperature.

Figure 12 shows that the domain of bistability shrinks as the temperature is increased and disappears above 520 K. This phenomenon can be explained by the acceleration of water formation as the temperature increases, which results into the depletion of oxygen, hence the decrease of the critical hydrogen pressure separating the bistable from the hydrogen-covered domain, as in the mean-field model [36].

The simulations are carried out for a tip radius of 19 nm in Fig. 12a, and for a tip radius of 15 nm in Fig. 12b. According to Table I, the numbers of sites available on the facets are larger for the larger radius. The stochasticity is thus higher for the smaller radius than for the larger. However, the difference is not significant, as seen in Fig. 12. The most pronounced effect is that the upper curve delimiting the bistability domain is shifted towards slightly larger values of hydrogen pressure for  $R = 15$  nm than for  $R = 19$  nm. Nevertheless, the main features are similar to those of the mean-field model, which shows that the results are not much sensitive to changes of about 25% in the radius of curvature.

Moreover, the simulations show that bistability persists if the electric field vanishes, but the domain of bistability

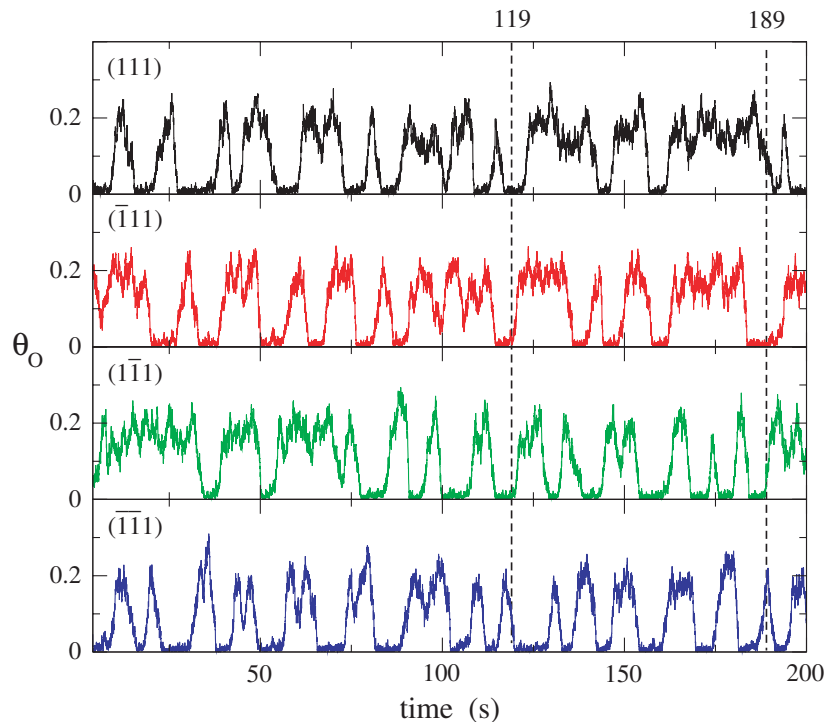


FIG. 13: Time series of the oxygen coverage  $\theta_{\text{O}}$  on the four  $\{111\}$  facets in the bistable regime for 450 K,  $P_{\text{O}_2} = 5.0 \times 10^{-4}$  Pa,  $P_{\text{H}_2} = 9.0 \times 10^{-4}$  Pa,  $F_0 = 12.3$  V/nm, and  $R = 19$  nm. The vertical lines are guides for the eye for time  $t = 119$  s and  $t = 189$  s.

becomes smaller as the electric field decreases [35].

#### D. Burst noise

Because of the stochasticity, the coverages erratically fluctuate in time. In the regime of bistability, the surface randomly switches between the hydrogen- and oxygen-covered states, a phenomenon which cannot be explained with a deterministic kinetic model.

As observed in the experiment (see Figs. 2-3), the four quadrants including the facets  $\{111\}$  switch between the two states independently of each other. This statistical independence between the quadrants can be understood as resulting from the barrier to hydrogen surface diffusion created by the cross-like oxidized zone.

In the simulations, the four quadrants correspond to large percolation clusters where  $\theta_{\text{O}} < 0.4$  and hydrogen diffusion is restricted to these percolation clusters, as explained in Section V. The four quadrants undergo desynchronized random switches, as shown in the simulation of Fig. 13. This figure depicts the time series of oxygen coverage in the four facets (111),  $(\bar{1}11)$ ,  $(1\bar{1}1)$ , and  $(\bar{1}\bar{1}1)$  at the center of the four quadrants. For each quadrant, the time series shows that the oxygen coverage randomly switches between a vanishing value corresponding to the hydrogen-covered state and a positive value for the oxygen-covered state. These random switches explain the burst noise observed in Fig. 3 for the brightness of one quadrant. Moreover, we observe in Fig. 13 that, at the same time, some facets may be in the hydrogen-covered state, while others are in the oxygen-covered one.

Two examples are given in Fig. 14 at the times  $t = 119$  s and  $t = 189$  s. Figures 14a & b show the percolation clusters formed at these times. Four of them are large and correspond to the four quadrants. Figures 14c & d depict the bright quadrants that are covered by hydrogen. At the time  $t = 119$  s, the quadrants with the facets  $(1\bar{1}1)$  and  $(\bar{1}\bar{1}1)$  are well covered by hydrogen and the quadrants with (111) and  $(\bar{1}11)$  mostly by oxygen, as seen in Fig. 14c. However, at the time  $t = 189$  s, only the quadrant with (111) is covered by hydrogen and the three others by oxygen, as seen in Fig. 14d. Therefore, the four quadrants turn out to be desynchronized, which is thus explained in the present stochastic model by the restriction of hydrogen diffusion within large percolation clusters.

In each quadrant, the burst noise can be characterized by the probability distribution  $p(\theta_{\text{O}})$  of oxygen coverage  $\theta_{\text{O}}(t)$  in time series. Figure 15 shows such probability distributions at three different temperatures for fixed hydrogen and oxygen pressures. As seen in Fig. 15, the probability distribution is bimodal at 440 K, which means that the

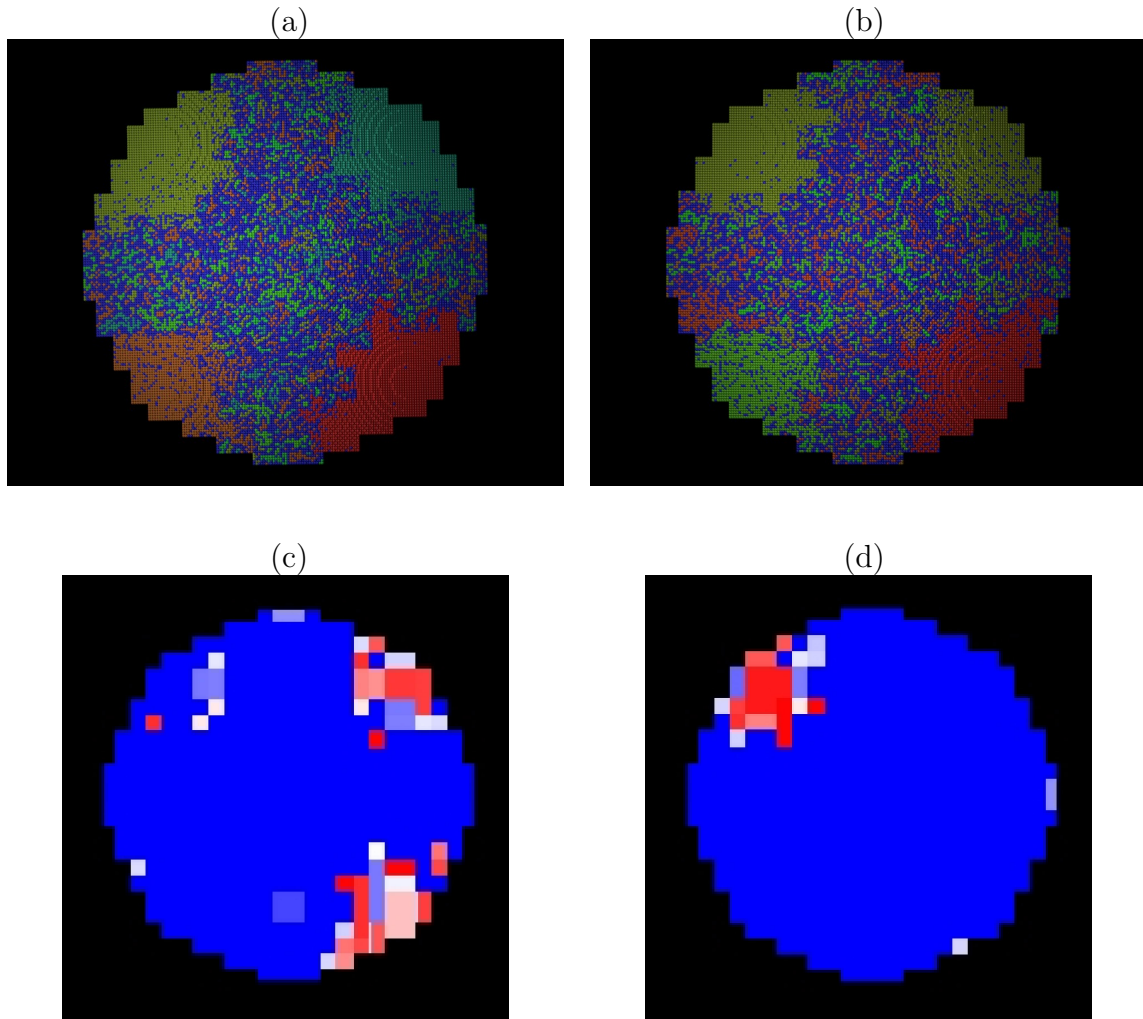


FIG. 14: Simulation of the surface coverage at the times: (a) & (c)  $t = 119$  s; (b) & (d)  $t = 189$  s in Fig. 13. In (a) & (b), the density of sites painted in dark (cross-like zone) is proportional to the oxygen coverage  $\theta_O$  of the underlying facet. In (c) & (d), the brightness is proportional to the hydrogen coverage  $\theta_H$ . Hydrogen diffuses rapidly and concentrates in large clusters of the nearest-neighboring facets with  $\theta_O < 0.4$  shown in (a) & (b) (forming the four quadrants and smaller clusters inside the cross-like zone). Images (c) & (d) compare with the top-left and top-right micrographs of Fig. 2.

distribution has two main peaks, showing that the quadrant has comparable probabilities to be in the hydrogen- and oxygen-covered states, as in the time series of Fig. 13. Instead, the surface is essentially covered by hydrogen at the high temperature of 480 K, because the probability distribution has its main peak around  $\theta_O \simeq 0.06$ . At the low temperature of 425 K, most of the probability is around  $\theta_O \simeq 0.47$ , which corresponds to the oxygen-covered state. If the probability distribution is essentially unimodal, as it is the case at 425 K and 480 K, the corresponding time series presents fluctuations around a single state (either the hydrogen- or the oxygen-covered state) and the noise is no longer of burst type.

Noticeably, the facet sizes of Table I yield the level of stochasticity required to understand the main features of the burst noise.

### E. Front propagation during transitions

The stochastic model also reproduces the phenomenon of front propagation observed in Fig. 4 during the transitions between the hydrogen- and oxygen-covered states. Figure 16a shows the simulated time dependence of the oxygen coverage in three facets (447), (557), and (111) along the diagonal of a quadrant, as seen in Fig. 16b. When the oxidized state invades the quadrant, these facets are successively switching to the oxygen-covered state in the temporal order

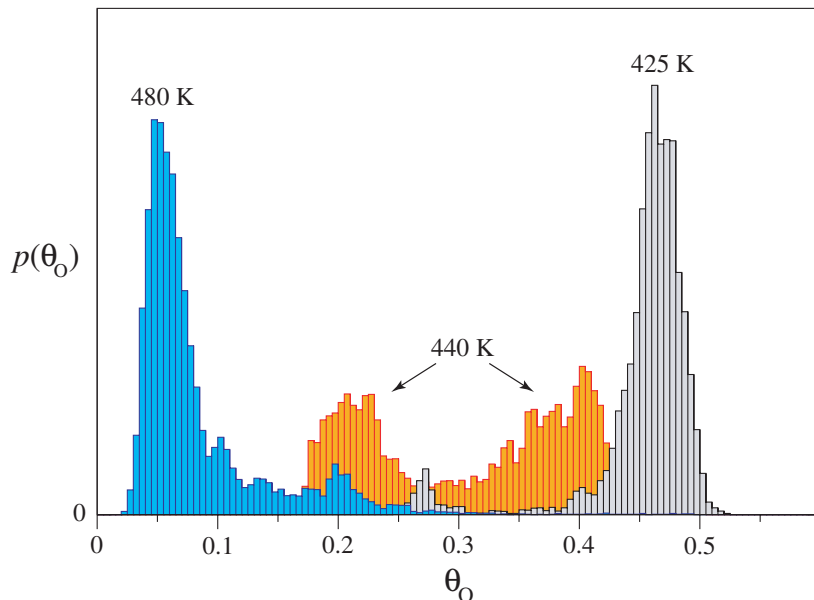


FIG. 15: Histograms giving the probability distributions of oxygen coverage,  $p(\theta_O)$ , at 480 K, 440 K, and 425 K (from left to right), obtained from time series for the number of sites occupied by oxygen in one quadrant (6962 sites, 40 facets) with the same conditions as in Fig. 13:  $P_{O_2} = 5.0 \times 10^{-4}$  Pa,  $P_{H_2} = 9.0 \times 10^{-4}$  Pa,  $F_0 = 12.3$  V/nm, and  $R = 19$  nm.

(447)  $\rightarrow$  (557)  $\rightarrow$  (111), as observed in Fig. 16a. Accordingly, the oxidation front propagates in the direction going from the apex towards the flanks, in agreement with the experimental observations of Fig. 4. As the quadrant returns to the metallic state, the reversed order (111)  $\rightarrow$  (557)  $\rightarrow$  (447) is followed, so that the oxidation front retracts.

The propagation speed is of the order of 10 nm/s. It is due to the nonuniformity of the rate processes taking place on the surface.

## IX. CONCLUSIONS

This paper presents a comprehensive understanding of burst noise in the bistable regime for the catalytic formation of water on a rhodium field emitter tip. Experimental observations of this system show a nanopattern composed of four quadrants undergoing random switches in time between hydrogen- and oxygen-covered states. To understand this fluctuating phenomenon, a stochastic approach has been developed extending our deterministic kinetic model [34–36]. This model could already explain the non-fluctuating phenomena observed in the experiment, including: (1) the nanopattern with a cross-like zone separating the four quadrants, which finds its origin in the spatial modulation of rate constants due to the anisotropy of the underlying crystal; (2) the role of the electric field to promote the oxidation of rhodium and the formation of the oxide trilayer O(ad)-Rh-O(sub); (3) the oscillations generated by inhibition of adsorption in the presence of the surface oxide; (4) the bistable regime itself with the hysteretic behavior between the hydrogen- and oxygen-covered states. However, as previously pointed out [35], the deterministic model left open the understanding of the burst noise observed in the bistable regime.

Now, we have been able to carry out the extension of the deterministic model into a stochastic model explaining not only the aforementioned non-fluctuating phenomena (1)-(4), but also the fluctuating phenomenon of burst noise in the regime of bistability.

In the stochastic model, the time evolution is numerically simulated for the random numbers of hydrogen, oxygen, and subsurface oxygen atoms in the facets composing the rhodium tip. These random numbers change in time due to the different adsorption, desorption, reaction, and diffusion processes. We have developed a stochastic algorithm to numerically simulate the overall time evolution at regular time steps  $\Delta t$  on the multifaceted surface.

For the processes of adsorption, desorption, and reaction, the algorithm consists in updating the random numbers by adding together multinomial random variables. This method has the advantage of simulating the processes with an equal time step  $\Delta t$ , while preserving the non-negativity of the random numbers of atoms.

To understand the burst noise, a key role is played by hydrogen diffusion, which is ultrafast on metallic surfaces. The present study shows that the overall ultrafast hydrogen redistribution assumed in previous work [34–36] cannot explain

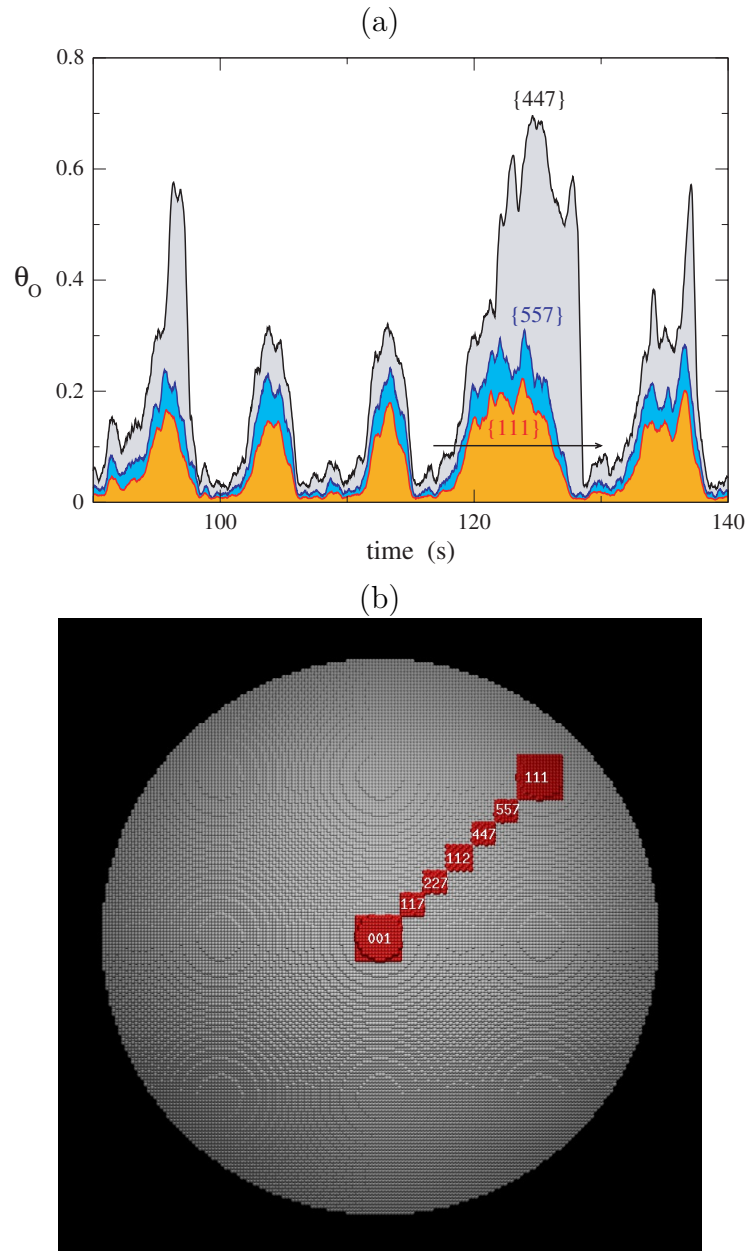


FIG. 16: (a) Time evolution of the oxygen coverage in the bistable regime on the facets  $\{111\}$  (lower curve),  $\{557\}$  (middle curve), and  $\{447\}$  (upper curve) showing the propagation of the oxygen-covered state in the same conditions as in Fig. 13. As shown by the arrow, the oxygen-covered state occupies successively the facets  $\{112\}$ ,  $\{447\}$ ,  $\{557\}$ ,  $\{111\}$  from the apex of the tip towards the flanks, and withdraws. (b) Schematic representation of these facets in a quadrant. Note that the hydrogen-covered state propagates in the opposite direction (see Fig. 4).

the burst noise observed in the bistability regime. Indeed, hydrogen diffusion is likely to be much reduced in the cross-like oxidized zone because the strongly bounded oxygen adatoms stop the hydrogen adatoms and, moreover, trigger water formation. Accordingly, hydrogen diffusion should be limited to percolation clusters where the oxygen coverage is below the percolation threshold. Consistently, the largest percolation clusters correspond to the four quadrants observed in the experiment. A special algorithm has been devised to numerically simulate hydrogen percolation at every time step  $\Delta t$ . This algorithm consists in, first, regrouping the facets having their oxygen coverage below threshold into percolation clusters and, secondly, redistributing the hydrogen adatoms inside each percolation cluster according to a Gibbsian canonical equilibrium distribution.

The numerical simulations are performed by alternating the random updates of the numbers of atoms in every

facets with hydrogen transport by percolation at each time step  $\Delta t$ . We notice that the fluctuations generated by this stochastic algorithm have amplitudes fixed by the atomic structure of the crystalline surface and the geometry of the field emitter tip. Indeed, the numbers of available sites in every facet are determined by the underlying crystal structure and the tip radius of curvature. Remarkably, this stochastic model can reproduce the nanopatterns, the oscillations, and the bistability diagram observed in the experiment, but also the key features of the burst noise in the bistable regime. In particular, the numerical simulations show that the noise manifests itself independently in the four quadrants, which undergo desynchronized random switches between the hydrogen- and oxygen-covered states, in agreement with the experimental observations. Moreover, the stochastic model also reproduces the phenomenon of front propagation observed when a quadrant rapidly switches from the oxygen- to the hydrogen-covered state or back, as seen in Fig. 4. This propagation is here understood as due to the nonuniformity of the characteristic properties of the surface.

To conclude, the stochastic model extends and completes our previous deterministic model in providing a comprehensive theory for the different phenomena observed by field ion microscopy in the catalytic formation of water on rhodium. This study opens important perspectives in the understanding of hydrogen diffusion on oxidized surfaces. The mechanism of percolation goes beyond the mean-field approach and appears to be of general interest. The interplay between this transport mechanism and the reactions taking place on the surface should be further investigated to obtain a systematic description of these fundamental processes.

### Acknowledgments

The authors thank Yannick De Decker, Jean-Sabin McEwen, and Miguel Pineda for helpful discussions and suggestions. This research is financially supported by the Wallonia-Brussels Federation (Action de Recherches Concertées No. AUWB 2010-2015/ULB15).

### APPENDIX A: HYDROGEN EQUILIBRIUM DISTRIBUTION

In this Appendix, we consider the equilibrium distribution of hydrogen adatoms over the  $n_j \equiv n$  facets  $\{i\}_{i=1}^n$  composing some percolation cluster  $j$ . The  $i^{\text{th}}$  facet has  $N_i$  available sites, among which  $0 \leq O_i \leq N_i$  are occupied by oxygen adatoms. The remaining sites may thus be occupied by  $0 \leq H_i \leq N_i - O_i$  hydrogen adatoms. The potential energy of all the hydrogen adatoms in the cluster is defined as  $U_{\text{tot}} = \sum_{i=1}^n U_{\text{Hi}} H_i$ , where  $U_{\text{Hi}}$  is the potential energy (32) of a hydrogen adatom bounded to the surface. The total number of hydrogen adatoms in the cluster takes the value  $H_{\text{tot}} = \sum_{i=1}^n H_i$ .

Counting the number of microstates such that  $\{H_i\}$  hydrogen adatoms occupy the  $\{N_i - O_i\}$  sites available in every facet, the canonical equilibrium distribution is expressed as

$$P_c(\{H_i\}) = \frac{1}{Z(H_{\text{tot}})} \prod_{i=1}^n \frac{(N_i - O_i)!}{H_i! (N_i - O_i - H_i)!} e^{-\beta U_{\text{Hi}} H_i}, \quad (\text{A1})$$

under the constraint of given total number  $H_{\text{tot}} = \sum_{i=1}^n H_i$ . In this regard, the canonical distribution is the conditional probability that the numbers of hydrogen adatoms in the facets take the values  $\{H_i\}$  given that their total number is equal to  $H_{\text{tot}}$ . In Eq. (A1),  $Z(H_{\text{tot}})$  denotes the partition function such that  $\sum_{\{H_i\}} P_c(\{H_i\}) = 1$ , and  $\beta = (k_B T)^{-1}$ .

If the mean hydrogen occupancy is small  $H_i \ll M_i \equiv N_i - O_i$ , we can use Stirling's formula and the approximation  $(1 - H_i/M_i)^{-M_i} \simeq e^{H_i}$  to get:

$$\frac{M_i!}{(M_i - H_i)!} \simeq \left(1 - \frac{H_i}{M_i}\right)^{-M_i} \left(\frac{M_i - H_i}{e}\right)^{H_i} \simeq (M_i - H_i)^{H_i}, \quad (\text{A2})$$

hence, Eq. (31).

It is important to compare with the grand-canonical equilibrium distribution

$$P_{\text{gc}}(\{H_i\}) = \prod_{i=1}^n \frac{(N_i - O_i)!}{H_i! (N_i - O_i - H_i)!} p_i^{H_i} (1 - p_i)^{N_i - O_i - H_i}, \quad (\text{A3})$$

with the site occupation probability

$$p_i = \frac{1}{1 + e^{\beta(U_{\text{Hi}} - \mu)}}, \quad (\text{A4})$$

and satisfying the normalization condition  $\sum_{\{H_i\}} P_{\text{gc}}(\{H_i\}) = 1$ . Accordingly, the mean hydrogen coverage is given by

$$\theta_{\text{Hi}} = \frac{\langle H_i \rangle}{N_i} = \frac{1 - \theta_{\text{Oi}}}{1 + e^{\beta(U_{\text{Hi}} - \mu)}}, \quad (\text{A5})$$

with  $\theta_{\text{Oi}} = O_i/N_i$ , as expected from previous work [34–36]. The grand-canonical distribution supposes that the total number of hydrogen adatoms fluctuates around its average value  $\langle H_{\text{tot}} \rangle = \sum_{i=1}^n \langle H_i \rangle$ , although the canonical distribution corresponds to the situation where the total number of hydrogen adatoms takes the given value  $H_{\text{tot}} = \sum_{i=1}^n H_i$ , as it is the case between any two adsorption-desorption-reaction events taking place on the surface. Consequently, we should here consider the canonical distribution. We notice that, if the total number of hydrogen adatoms is large, its value can be approximated by the relation  $H_{\text{tot}} \simeq \sum_{i=1}^n N_i \theta_{\text{Hi}}$  using Eq. (A5). *Vice versa*, this relation can be inverted to obtain the value of the chemical potential  $\mu$  corresponding to the total number  $H_{\text{tot}}$ . In this way, the chemical potential used in previous work [34–36] is recovered.

## APPENDIX B: STOCHASTIC ALGORITHM IN A SINGLE FACET

Here, we present the part of the stochastic algorithm corresponding to the updates of the numbers of hydrogen adatoms  $H \equiv H_i$ , oxygen adatoms  $O \equiv O_i$ , and subsurface oxygen atoms  $S \equiv S_i$  due to adsorption, desorption, and reaction in a single facet  $i$ :

$$P_{t+\Delta t} \Big|_i \simeq \exp\left(\hat{L}_{\text{adr},i} \Delta t\right) P_t. \quad (\text{B1})$$

We denote by  $N \equiv N_i$  the number of sites available in this facet.

First, we notice that the mean-field kinetic equations for adsorption, desorption, and reaction, which we have already obtained in previous work [34–36], can be written as follows in terms of the mean occupation numbers (2):

$$\frac{d\theta_{\text{H}}}{dt} = k_{+\text{H}}(1 - \theta_{\text{H}} - \theta_{\text{O}}) - k_{-\text{H}}\theta_{\text{H}}, \quad (\text{B2})$$

$$\frac{d\theta_{\text{O}}}{dt} = k_{+\text{O}}(1 - \theta_{\text{H}} - \theta_{\text{O}}) - k_{-\text{O}}\theta_{\text{O}}, \quad (\text{B3})$$

$$\frac{d\theta_{\text{S}}}{dt} = k_{+\text{S}}(1 - \theta_{\text{S}}) - k_{-\text{S}}\theta_{\text{S}}, \quad (\text{B4})$$

with the following coefficients:

$$k_{+\text{H}} = 2k_{\text{aH}}P_{\text{H}_2}\theta_{\emptyset}, \quad (\text{B5})$$

$$k_{-\text{H}} = 2k_{\text{dH}}\theta_{\text{H}} + 2k_{\text{r}}\theta_{\text{O}}, \quad (\text{B6})$$

$$k_{+\text{O}} = 2k_{\text{aO}}P_{\text{O}_2}\theta_{\emptyset} + k_{\text{red}}\theta_{\text{S}}, \quad (\text{B7})$$

$$k_{-\text{O}} = 2k_{\text{dO}}\theta_{\text{O}} + k_{\text{ox}}(1 - \theta_{\text{S}}) + k_{\text{r}}\theta_{\text{H}}, \quad (\text{B8})$$

$$k_{+\text{S}} = k_{\text{ox}}\theta_{\text{O}}, \quad (\text{B9})$$

$$k_{-\text{S}} = k_{\text{red}}\theta_{\emptyset}, \quad (\text{B10})$$

the dihydrogen and dioxygen pressures (4), the rate constants (12), (13), (17), (18), (23), (24), (26), and  $\theta_{\emptyset} = 1 - \theta_{\text{H}} - \theta_{\text{O}}$ .

If the time step  $\Delta t$  is small enough, we can use Eqs. (B2)-(B4) as the template for the stochastic process defined by supposing that the coefficients (B5)-(B10) remain unchanged during the time interval  $[t, t + \Delta t]$ .

The remarkable result is that the stochastic processes of such linear kinetic equations can be solved exactly [69].

Since Eqs. (B2)-(B3) are decoupled from Eq. (B4) in the linear approximation, the update of the numbers  $(H, O)$  can be performed independently of the update of  $S$ .

The number  $S$  of subsurface oxygen atoms is updated according to

$$S \longrightarrow \mathcal{B}[S, Sp_{\text{S}} + S(1 - p_{\text{S}})e^{-k_{\text{S}}\Delta t}] + \mathcal{B}[N - S, (N - S)p_{\text{S}}(1 - e^{-k_{\text{S}}\Delta t})], \quad (\text{B11})$$

where

$$k_{\text{S}} = k_{+\text{S}} + k_{-\text{S}}, \quad p_{\text{S}} = \frac{k_{+\text{S}}}{k_{+\text{S}} + k_{-\text{S}}}, \quad (\text{B12})$$

and  $X = \mathcal{B}(N, A) \in [0, N]$  denotes an integer random variable obeying the binomial probability distribution

$$P(X) = \frac{N!}{X!(N-X)!} p^X (1-p)^{N-X} \quad (\text{B13})$$

of mean value  $A = \langle X \rangle = Np$ . In Eq. (B11), the two binomial random variables are statistically independent. Since each binomial deviate is non negative, the update of  $S$  given by the sum (B11) of two binomial deviates is always non negative. Moreover, the first binomial random variable belongs to the interval  $[0, S]$  and the second to  $[0, N - S]$  so that their sum remains in the interval  $[0, N]$  without exceeding the maximum number  $N$  of available sites, as it should.

Next, the numbers  $H$  and  $O$  of hydrogen and oxygen adatoms can be updated similarly as

$$\begin{aligned} \{H, O\} \longrightarrow & \mathcal{T} \left[ H, H p_{\text{H}}^{(1)}(\Delta t), H p_{\text{O}}^{(1)}(\Delta t) \right] \\ & + \mathcal{T} \left[ O, O p_{\text{H}}^{(2)}(\Delta t), O p_{\text{O}}^{(2)}(\Delta t) \right] \\ & + \mathcal{T} \left[ N - H - O, (N - H - O) p_{\text{H}}^{(3)}(\Delta t), (N - H - O) p_{\text{O}}^{(3)}(\Delta t) \right], \end{aligned} \quad (\text{B14})$$

where  $\{X, Y\} = \mathcal{T}(N, \langle X \rangle, \langle Y \rangle)$  denotes a pair of integer random variables  $X \in [0, N]$  and  $Y \in [0, N]$  obeying the trinomial probability distribution:

$$P(X, Y) = \frac{N!}{X! Y! (N - X - Y)!} p_{\text{X}}^X p_{\text{Y}}^Y (1 - p_{\text{X}} - p_{\text{Y}})^{N - X - Y} \quad (\text{B15})$$

of mean values  $\langle X \rangle = Np_{\text{X}}$  and  $\langle Y \rangle = Np_{\text{Y}}$ . For  $i = 1, 2, 3$ , the quantities  $p_{\text{H}}^{(i)}(\Delta t)$  and  $p_{\text{O}}^{(i)}(\Delta t)$  are given by

$$\begin{pmatrix} p_{\text{H}}^{(i)}(\Delta t) \\ p_{\text{O}}^{(i)}(\Delta t) \end{pmatrix} = \begin{pmatrix} c_{\text{H}} \\ c_{\text{O}} \end{pmatrix} + e^{-\mathbf{K}\Delta t} \begin{pmatrix} p_{\text{H}}^{(i)}(0) - c_{\text{H}} \\ p_{\text{O}}^{(i)}(0) - c_{\text{O}} \end{pmatrix} \quad (\text{B16})$$

with the matrix

$$\mathbf{K} = \begin{pmatrix} k_{+\text{H}} + k_{-\text{H}} & k_{+\text{H}} \\ k_{+\text{O}} & k_{+\text{O}} + k_{-\text{O}} \end{pmatrix}, \quad (\text{B17})$$

the parameters

$$\begin{pmatrix} c_{\text{H}} \\ c_{\text{O}} \end{pmatrix} = \mathbf{K}^{-1} \begin{pmatrix} k_{+\text{H}} \\ k_{+\text{O}} \end{pmatrix}, \quad (\text{B18})$$

and the initial conditions:

$$p_{\text{H}}^{(1)}(0) = 1, \quad p_{\text{O}}^{(1)}(0) = 0, \quad (\text{B19})$$

$$p_{\text{H}}^{(2)}(0) = 0, \quad p_{\text{O}}^{(2)}(0) = 1, \quad (\text{B20})$$

$$p_{\text{H}}^{(3)}(0) = 0, \quad p_{\text{O}}^{(3)}(0) = 0. \quad (\text{B21})$$

We notice that Eqs. (B16)-(B18) give the solutions of Eqs. (B2)-(B3) considered as linear equations and starting from the initial conditions  $p_{\text{H}}^{(i)}(0)$  and  $p_{\text{O}}^{(i)}(0)$ . These solutions rule the time evolution of the mean values of the trinomial random variables determining the update of hydrogen and oxygen. The numbers of adatoms always remain in the intervals  $H \in [0, N]$  and  $O \in [0, N]$  because the update is constructed as a sum of three trinomial pairs of maximum values  $H$ ,  $O$ , and  $N - H - O$ , summing to the maximum value  $N$ .

The algorithm is first-order accurate in the time step  $\Delta t$  and is preserving the non-negativity of the numbers  $H$ ,  $O$ , and  $S$ .

These updates are performed for every one of all the facets  $\{i\}_{i=1}^n$  composing the tip surface, before redistributing the hydrogen adatoms, as explained in Sections V and VI.

---

[1] G. Nicolis and I. Prigogine, *Self-Organization in Nonequilibrium Systems* (Wiley, New York, 1977).

- [2] I. R. Epstein and K. Showalter, *J. Phys. Chem.* **100**, 13132 (1996).
- [3] M. T. M. Koper, *J. Chem. Soc. Faraday Trans.*, **94**, 1369 (1998).
- [4] A. De Wit, *Adv. Chem. Phys.* **109**, 435 (1999).
- [5] M. Eiswirth and G. Ertl, *Surf. Sci.* **177**, 90 (1986).
- [6] S. Jakubith, H. H. Rotermund, W. Engel, A. von Oertzen, and G. Ertl, *Phys. Rev. Lett.* **65**, 3013 (1990).
- [7] R. Imbihl and G. Ertl, *Chem. Rev.* **95**, 697 (1995).
- [8] R. Imbihl, *Surf. Sci.* **603**, 1671 (2009).
- [9] J.-S. McEwen, P. Gaspard, Y. De Decker, C. Barroo, T. Visart de Bocarmé, and N. Kruse, *Langmuir* **26**, 16381 (2010).
- [10] T. Visart de Bocarmé, T. Bär, and N. Kruse, *Ultramicroscopy* **89**, 75 (2001).
- [11] T. Visart de Bocarmé, G. Beketov, and N. Kruse, *Surf. Interface Anal.* **36**, 522 (2004).
- [12] M. F. H. van Tol, A. Gielbert, and B. E. Nieuwenhuys, *Catal. Lett.* **16**, 297 (1992).
- [13] V. Gorodetskii, J. H. Block, and M. Ehsasi, *Appl. Surf. Sci.* **67**, 198 (1992).
- [14] V. Gorodetskii, W. Drachsel, and J. H. Block, *Catal. Lett.* **19**, 223 (1993).
- [15] V. Gorodetskii, J. Lauterbach, H.-H. Rotermund, J. H. Block, and G. Ertl, *Nature* **370**, 276 (1994).
- [16] N. Ernst, G. Bozdech, V. Gorodetskii, H.-J. Kreuzer, R. L. C. Wang, and J. H. Block, *Surf. Sci.* **318**, L1211 (1994).
- [17] C. Voss and N. Kruse, *Appl. Surf. Sci.* **94/95**, 186 (1996).
- [18] N. Kruse and T. Visart de Bocarmé, in: G. Ertl, H. Knözinger, F. Schüth, and J. Weitkamp, Editors, *Handbook of Heterogeneous Catalysis*, 2nd edition (Wiley-VCH, Weinheim, 2008) pp. 870-895.
- [19] H. Malchow and L. Schimansky-Geier, *Noise and Diffusion in Bistable Nonequilibrium Systems* (Teubner Verlag, Leipzig, 1986).
- [20] K. Fichtorn, E. Gulari, and R. Ziff, *Phys. Rev. Lett.* **63**, 1527 (1989).
- [21] P. Hänggi, P. Talkner, and M. Borkovec, *Rev. Mod. Phys.* **62**, 251 (1990).
- [22] V. P. Zhdanov and B. Kasemo, *Surf. Sci. Rep.* **20**, 111 (1994).
- [23] V. P. Zhdanov, *Surf. Sci. Rep.* **45**, 231 (2002).
- [24] Yu. Suchorski, J. Beben, and R. Imbihl, *Prog. Surf. Sci.* **59**, 343 (1998).
- [25] Yu. Suchorski, J. Beben, and R. Imbihl, *Surf. Sci.* **454-456**, 331 (2000).
- [26] Yu. Suchorski, J. Beben, E. W. James, J. W. Evans, and R. Imbihl, *Phys. Rev. Lett.* **82**, 1907 (1999).
- [27] Yu. Suchorski, J. Beben, R. Imbihl, E. W. James, D.-J. Liu, and J. W. Evans, *Phys. Rev. B* **63**, 165417 (2001).
- [28] D.-J. Liu and J. W. Evans, *J. Chem. Phys.* **117**, 7319 (2002).
- [29] V. Johánek, M. Laurin, A. W. Grant, B. Kasemo, C. R. Henry, and J. Libuda, *Science* **304**, 1639 (2004).
- [30] D.-J. Liu and J. W. Evans, *Prog. Surf. Sci.* **88**, 393 (2013).
- [31] M. Pineda, L. Schimansky-Geier, and R. Imbihl, *Phys. Rev. E* **75**, 061107 (2007).
- [32] X. Guo, Y. De Decker, and J. W. Evans, *Phys. Rev. E* **82**, 021121 (2010).
- [33] N. Pavlenko, J. W. Evans, D.-J. Liu, and R. Imbihl, *Phys. Rev. E* **65**, 016121 (2001).
- [34] J.-S. McEwen, P. Gaspard, T. Visart de Bocarmé, and N. Kruse, *Proc. Natl. Acad. Sci. USA* **106**, 3006 (2009).
- [35] J.-S. McEwen, P. Gaspard, T. Visart de Bocarmé, and N. Kruse, *J. Phys. Chem. C* **113**, 17045 (2009).
- [36] J.-S. McEwen, P. Gaspard, T. Visart de Bocarmé, and N. Kruse, *Surf. Sci.* **604**, 1353 (2010).
- [37] A. Gaussmann and N. Kruse, *Catal. Lett.* **10**, 305 (1991).
- [38] M. K. Miller, A. Cerezo, M. G. Hetherington, and G. D. W. Smith, *Atom Probe Field Ion Microscopy: Monographs on the Physics and Chemistry of Materials* (Clarendon Press, Oxford, 1996).
- [39] E. A. Guggenheim, in: S. Flügge, Editor, *Encyclopedia of Physics*, Vol. III/2 (Springer Verlag, Berlin, 1959) pp. 1-118.
- [40] N. D. Bridge and A. D. Buckingham, *Proc. R. Soc. Lond. A* **295**, 334 (1966).
- [41] F. C. von der Lage and H. A. Bethe, *Phys. Rev.* **71**, 612 (1947).
- [42] H. J. Kreuzer, in: Ph. Avouris, Editor, *Atomic and Nanometer-Scale Modification of Materials: Fundamentals and Applications* (Kluwer, Dordrecht, 1993) pp. 75-86.
- [43] S. H. Payne, H. J. Kreuzer, W. Frie, L. Hammer, and K. Heinz, *Surf. Sci.* **421**, 279 (1999).
- [44] W. Nichtl-Pecher, *Ph.D. thesis* (University of Erlangen, Nürnberg, 1990).
- [45] J. T. Yates, P. A. Thiel, and W. H. Weinberg, *Surf. Sci.* **84**, 427 (1979).
- [46] A. N. Salanov and V. I. Savchenko, *Surf. Sci.* **296**, 393 (1993).
- [47] G. B. Fisher and S. J. Schmieg, *J. Vac. Sci. Technol. A* **1**, 1064 (1983).
- [48] E. Schwarz, J. Lenz, H. Wohlgemuth, and K. Christmann, *Vacuum* **41**, 167 (1990).
- [49] K. A. Peterlinz and S. J. Sibener, *J. Phys. Chem.* **99**, 2817 (1995).
- [50] J. Gustafson, A. Mikkelsen, M. Borg, E. Lundgren, L. Köhler, G. Kresse, M. Schmid, P. Varga, J. Yuhara, X. Torrelles, C. Quirós, and J. N. Andersen, *Phys. Rev. Lett.* **92**, 126102 (2004).
- [51] L. Köhler, G. Kresse, M. Schmid, E. Lundgren, J. Gustafson, A. Mikkelsen, M. Borg, J. Yuhara, J. N. Andersen, M. Marsman, and P. Varga, *Phys. Rev. Lett.* **93**, 266103 (2004).
- [52] J. Gustafson, A. Mikkelsen, M. Borg, J. N. Andersen, E. Lundgren, C. Klein, W. Hofer, M. Schmid, P. Varga, L. Köhler, G. Kresse, N. Kasper, A. Stierle, and H. Dosch, *Phys. Rev. B* **71**, 115442 (2005).
- [53] C. Dri, C. Africh, F. Esch, G. Comelli, O. Dubay, L. Köhler, F. Mittendorfer, G. Kresse, P. Dubin, and M. Kiskinova, *J. Chem. Phys.* **125**, 094701 (2006).
- [54] F. Mittendorfer, *J. Phys. Condens. Matter* **22**, 393001 (2010).
- [55] J.-S. McEwen, P. Gaspard, F. Mittendorfer, T. Visart de Bocarmé, and N. Kruse, *Chem. Phys. Lett.* **452**, 133 (2008).
- [56] F. Che, S. Ha, and J.-S. McEwen, *Catalytic Water Dehydrogenation and Formation on Nickel: Dual Path Mechanism in High Electric Fields*, submitted to *Journal of Catalysis* (2015).

- [57] L. Gregoratti, A. Baraldi, V. R. Dhanak, G. Comelli, M. Kiskinova, and R. Rosei, *Surf. Sci.* **340**, 205 (1995).
- [58] A. Makeev and R. Imbihl, *J. Chem. Phys.* **113**, 3854 (2000).
- [59] A. Schaak and R. Imbihl, *J. Chem. Phys.* **113**, 9822 (2000).
- [60] J. W. Evans, D.-J. Liu, and M. Tammara, *Chaos* **12**, 131 (2002).
- [61] D.-J. Liu and J. W. Evans, *J. Chem. Phys.* **113**, 10252 (2000).
- [62] D. Stauffer and A. Aharony, *Introduction to Percolation Theory*, 2nd edition (Taylor & Francis, London, 1992).
- [63] M. Sahimi, *Applications of Percolation Theory* (Taylor & Francis, London, 1994).
- [64] I. Webman, *Phys. Rev. Lett.* **47**, 1496 (1981).
- [65] B. Derrida, R. Orbach, and K.-W. Yu, *Phys. Rev. B* **29**, 6645 (1984).
- [66] A. Mikhailov and G. Ertl, *Chem. Phys. Lett.* **238**, 104 (1995).
- [67] D. T. Gillespie, *J. Comput. Phys.* **22**, 403 (1976).
- [68] D. T. Gillespie, *J. Phys. Chem.* **81**, 2340 (1977).
- [69] C. W. Gardiner, *Handbook of Stochastic Methods*, 3rd edition (Springer Verlag, Berlin, 2004).